Simultaneous occurrence of Traveling Ionospheric Disturbances, Farley Buneman and Gradient Drift Instabilities observed by the Zhongshan SuperDARN HF radar

Alicreance HIYADUTUJE [1], John Bosco Habarulema [1,2], Michael J. Kosch [1,3,4], Xiangcai Chen [5,6], Judy A. E. Stephenson [3], Tshimangadzo Merline Matamba [1]

[1]South African National Space Agency (SANSA), Hermanus, South Africa
[2]Department of Physics and Electronics, Rhodes University, Makhanda, South Africa
[3]Department of Chemistry and Physics, University of KwaZulu Natal (UKZN), Durban, South Africa
[4]Department of Physics, University of Lancaster, UK
[5]MNR Center for Space Physics and Astronomy, Polar Research Institute of China, Shanghai, China
[6]Antarctic Zhongshan Ice and Space Environment National Observation and Research Station, Polar Research Institute of China, Shanghai, China

Key Points:

- First demonstration of TIDs partially modulating Farley Buneman (FB) and Gradient Drift (GD) waves
- Farley Buneman and Gradient Drift Instabilities generate NREs
- Spearman rank correlation analysis shows that statistically ∼9% of NRE amplitude modulation could be due to MSTIDs.

Corresponding author: Alicreance HIYADUTUJE, hiyadutujea@yahoo.fr

Abstract

We show that Traveling Ionospheric Disturbances (TIDs) may affect the Farley Buneman Instability (FBI) and Gradient Drift Instability (GDI) echoes referred to as the Near Range Echoes (NREs) in the SuperDARN radar backscatter from the lower part of the E-region. TIDs and NREs are observed concomitantly by the Zhongshan SuperDARN radar (69.38° S, 76.38° E) in the far and near ranges, respectively. At the moment, there is no study about the effects of TIDs on the NREs caused by the FBI using the SuperDARN radars. The GDI are more likely to occur at a lower altitude while FBI occurs at a slightly higher altitude in the lower part of the ionospheric E-region. We use the Spearman Correlation Coefficient (SCC) to show that a part of the NREs backscatter power could be statistically explained by the MSTIDs backscatter power received by the same radar.

We also investigate the simultaneous occurrence rate of the NREs and MSTIDs during the 24^{th} solar cycle. Seasonal variability shows that MSTIDs-NREs events over Zhongshan mostly occur in summer and equinoxes during local night and morning. The majority of these events lasted between ∼4 and ∼8 hours. Most events disappeared early in the morning. Statistics of the Spearman correlation coefficient values show that ∼9% of NRE amplitude modulation could be due to the MSTIDs. There are almost equal numbers of negative and positive Spearman correlation coefficient values. The relative velocity between the E-region NREs and the F-region MSTIDs switching the electric field polarities between the crests and troughs could be the cause of those equal number of the Spearman correlation coefficient values. The orientation of the ionospheric current relative to the MSTID polarization electric field may also play a significant role in the reported Spearman correlation coefficient values. We argue that in some cases, the TIDs might have been close enough to the NREs altitude to modulate them directly by transporting the plasma up and down through shear or compression.

Plain Language Summary

SuperDARN radar Near Range Echoes (NREs) were observed at an altitude range of 95 - 125 km and are caused by the Gradient Drift Instability (GDI) and Farley Buneman Instability (FBI). Medium Scale Traveling Ionospheric Disturbances (MSTIDs) are wave-like perturbations of plasma density that propagate in the ionosphere. They are caused by any major ionospheric energy input such as the Atmospheric Gravity Waves (AGWs), Joule heating, Perkins instability, etc. It was argued that the MSTIDs partially modulate the NREs backscatter power associated with the GDI through the polarization electric field. We use the Zhongshan SuperDARN radar to show that apart from GDI, FBI related echoes are also partially modulated by the MSTIDs. We also record the number of MSTID-NRE events during 2010 - 2019 and found that the majority of them occurs in summer and equinoxes during local night and morning while the minority occurred in the winter of the southern hemisphere. We also perform a statistical study of the Spearman correlation coefficient values of all events recorded for this study.

1 Introduction

The Super Dual Auroral Radar Network (SuperDARN) High Frequency (HF) Near Range Echoes (NREs) are the backscatter received by the near range gates of each radar, i.e., in the range less than 350 km (Hall et al., 1997; Jenkins & Jarvis, 1999; Hussey et al., 2000). Examples of these echoes are: High-Aspect Angle Irregularity Region (HAIR) (Milan & Lester, 2001; Milan et al., 2004; Drexler & St-Maurice, 2005) and Far-Aspect Angle Irregularities Region (FAIR) echoes (St.-Maurice & Nishitani, 2020). In FAIR and HAIR echoes the aspect angle should be large, i.e, the modes must be decaying (Drexler & St-Maurice, 2005). In this case, the spectral width would be narrow indicating that there is no turbulence. The decaying modes are due to an altitude-dependent frequency implying that the aspect angle should increase monotonically with time and decrease the amplitude of the unstable modes. During the unstable stage, the growth rate must be large enough to compensate the decay of the observed modes so that the large amplitude could be observed (St.-Maurice & Nishitani, 2020).

HAIR echoes are associated with the Farley Buneman Instability (FBI) (Farley Jr, 1963; Buneman, 1963). They are linked to the relative velocity between the E-region ion drift and electron drift exceeding the ion acoustic speed (C_s) (Drexler & St-Maurice, 2005). FAIR echoes are caused by gradient drift instabilities (GDI) and are associated with the zonal neutral wind, meridional electric field and plasma density gradients (St.-Maurice & Nishitani, 2020; Hiyadutuje et al., 2022). For frequencies of the order of $\mathbf{k}\cdot\mathbf{V_i}$ which is too small for the modes to be of FBI, St.-Maurice and Nishitani (2020) introduced the GDI mechanism at the bottom-side of the E-region due to its steep gradients. A two-step process was involved: first, a 1 to 10 km scale GDI must be triggered by the density gradient, meridional electric field and zonal neutral wind. The instability would then push the upper part of the bottom-side high electron density to a region where there is a lower density. At the horizontal edges of these 1 - 10 km structures of 100 m scale gradients are formed and cascade to a $\sim$10 m finger-like irregularities that are observed by the SuperDARN radar. Apart from HAIR and FAIR echoes, there are five other types of NREs.

Other spectral types observed by the SuperDARN HF radars include: type Ia, type Ib, type II, type III, and type IV waves.

1. Type I waves are produced for wave vector directions for which the plasma is expected to be linearly unstable. There can be two types of type I, particularly if we pay attention to decameter structures, namely: Type Ia caused by the FBI and Type Ib caused by the GDI. At high latitudes, initially unstable waves, once they reach a large amplitude, are observed by radars to move at the instability threshold speed. This means that as the amplitude grows, the electric field inside the structures goes down (e.g., St.-Maurice & Hamza, 2001). If we have FBI, the waves will move at C_s. However, if we have GDI, the waves could have a Doppler shift that would be either larger than C_s or smaller than C_s. Such features have in fact been observed by SuperDARN and have been associated with 20 to 30 km plasma density gradients in the direction perpendicular to the geomagnetic field (St.-Maurice et al., 1994).
2. Type II waves are produced by mode-coupling. They are triggered in directions for which the plasma is stable, according to linear theory. The most important form of mode-coupling in the FBI and GDI involves coupling between wave vectors in the unstable direction and wave-vectors perpendicular to it (e.g., Sato, 1973; Sahr & Fejer, 1996; Otani & Oppenheim, 2006). Being the bi-product of turbulence they decay quickly, their spectrum is wide and their power less than for type I spectra. Being the bi-product of coupling involving modes perpendicular to the unstable directions, they will also only be observed in linearly stable directions.
3. Radars also observe very narrow spectra. Slow narrow spectra have inherited the un-original label “type III”. Consistent with this simple nomenclature, fast narrow spectra have been called “type IV”. The term “narrow” is important: the spectra are associated with weak turbulence and offer the best chance to study eigenmodes excited in threshold directions (or under extremely weak instability conditions). St.-Maurice and Chau (2016) showed how modes excited on the edge of the instability “cone” could go much faster than the ion-acoustic speed if the electric field was strong. Doppler shift of narrow spectra observed by Very High Frequency (VHF) instruments can be explained by the model involving the electron temperature and ion frictional heating when electric field is strong (St-Maurice et al., 2023).

There is a role played by ions, electrons, magnetic and electric fields to generate the E-region FBI and GDI. In the lower part of the ionospheric E-region, ions are unmagnetized, i.e., $\nu_{in}/\Omega_i > 1$, where ν_{in} is the ion-neutral collision frequency and Ω_i is the ion gyro-frequency (Kovalev et al., 2008; Rojas & Hysell, 2021). They move with the neutral atmosphere which sometimes is assumed to be stationary (Milan & Lester, 2001, and references therein), but the electrons are magnetized, i.e., $\nu_{en}/\Omega_e << 1$, where ν_{en} is the electron-neutral collision frequency and Ω_e is the electron gyro-frequency, and their motions are mainly governed by the electric and magnetic fields (Kovalev et al., 2008; Rojas & Hysell, 2021). There is a relative drift between the two species. This relative motion between the ions and electrons creates a drift current perpendicular to the magnetic field which is directly proportional to the electron density (St.-Maurice et al., 1986; Milan & Lester, 2001). This current is involved in the development of the FBI which generates the HAIR echoes observed by SuperDARN (Milan & Lester, 2001). For FBI to be observed by HF radars, an electric field of >40 mV/m is required (Hamza & St-Maurice, 1993; St.-Maurice et al., 1994; St.-Maurice, 1985; Kovalev et al., 2008; St.-Maurice & Nishitani, 2020). GDI responsible for the FAIR echoes can take place even when the electric field magnitude is small as long as its vector and an electron density gradient are in directions favourable to trigger the instability in a magnetic field (St.-Maurice & Nishitani, 2020).

The solution of the FBI and GDI dispersion relation is a complex frequency ($\omega(k)$) given by the equation (1)

$$\omega(k) = \omega(k)_r + i\gamma_k. \tag{1}$$

The real part of equation (1), $\omega(k)_r$ is used to predict the frequency of narrow spectra and is given by equation (2) (e.g., Fejer & Kelley, 1980; St.-Maurice, 1985; M. C. Kelley, 2009; Kelly, 2012; Rojas & Hysell, 2021):

$$\omega(k)_r = \frac{\mathbf{k} \cdot \mathbf{V}_d}{1+\psi}, \tag{2}$$

where $\mathbf{k}$ is the wavenumber vector and the term with the drift velocity ($\mathbf{V}_d$) is defined by equation (3) (St.-Maurice, 1985),

$$\mathbf{k} \cdot \mathbf{V}_d = k_y \frac{E}{B}. \tag{3}$$

If the altitude is higher or the electric field is very strong, $\omega(k)_r$ will have an additional $\mathbf{k} \cdot \mathbf{V_i}$ term. Equation (2) can only be used to check if there is a strong unstable situation, i.e., a frequency from linear theory that exceeds kC_s by a large factor. The nonlinearity then changes the frequency spectrum in such a way that for large amplitude modes, the average frequency of the widened spectrum is given by the $\gamma_k = 0$ (Hamza & St-Maurice, 1993). $\psi = \frac{\nu_{en}\nu_{in}}{\Omega_e \Omega_i}$, where $\nu_{en,in}$ are the collision frequencies of neutrals-electrons and neutrals-ions. The imaginary part of the equation (1) defines their growth rate (γ_k), which is given by equation (4) (M. C. Kelley, 2009; Rojas & Hysell, 2021):

$$\gamma_k = \frac{\psi}{(1+\psi)\nu_{in}} \left(\omega^2(k)_r - k^2 C_s^2 \right) + \frac{\nu_{in}}{\Omega_i} \frac{\omega(k)_r k_E}{Lk^2} - 2\alpha n_e \tag{4}$$

where k, k_E, V_d, $C_s = \sqrt{(\gamma_i T_i + \gamma_e T_e)/m_i}$, L, α, and n_e are the wavenumber, wave vector component in the direction of the background electric field, electron advection speed, ion acoustic speed, the scale length of density gradient, dissociative recombination rate, and electron density, respectively. The terms $\gamma_{i,e}$, $T_{i,e}$ and m_i are the ratio of a specific heat at constant pressure and specific heat at constant volume of species (i, e), temperature of species and the mass of ion (Hamza & St-Maurice, 1993). Note that at the altitude below 100 km, non-isothermal effects in electrons can increase the threshold magnitude of the speed in the $\mathbf{E}\times\mathbf{B}$ direction, but decrease or increase it further in other directions (Dimant & Sudan, 1995; Kissack et al., 1997; Dimant & Oppenheim, 2004;

Kissack et al., 2008). As a result, heat flow, inelastic collisions with neutrals, and heating modulation would affect the waves. We can neglect the term $(-2\alpha n_e)$ in the equation (4), because its contribution to the growth rate is very small at decameter and smaller sizes (Rojas & Hysell, 2021). The unitless constant ψ is defined by:

$$\psi(\theta) = \frac{\nu_{en}\nu_{in}}{\Omega_e \Omega_i}\left(1 + \frac{\Omega_e^2}{\nu_{en}^2}\theta^2\right) \tag{5}$$

where $\Omega_{e,i}$ and θ are the gyro-frequencies and the complement of the angle between $\mathbf{k}$ and the magnetic field $\mathbf{B}$, respectively. When $\theta = 0$, it means that $k \perp B$ and in this case, $\psi(0) \approx (\nu_{en}\nu_{in})/(\Omega_e\Omega_i)$. The first term on the right-hand side of the equation (4) describes the growth rate of the Farley Buneman waves (Fejer & Kelley, 1980; M. C. Kelley, 2009) while the second term defines the growth rate of the gradient drift waves. In the case of FBI, i.e., where the density gradient is negligible, the threshold electron velocity is $V_{eo} = C_s(1 + \psi(0))$ (John & Saxena, 1975), which gives $V_{eo} \approx C_s \approx 400$ m/s when $\psi(0) << 1$. There are many theoretical and numerical studies of the processes affecting the evolution of the FBI and GDI (e.g., Oppenheim & Dimant, 2013; Makarevich, 2016; Young et al., 2017, 2019; Makarevich, 2021).

On the other hand, occasionally TIDs may occur in the ionosphere and they have different scales based on their characteristics. TIDs are wave-like perturbations of the plasma, mainly generated by the Atmospheric Gravity Waves (AGWs) and the Perkins instability (Hunsucker, 1982; Miyoshi et al., 2018; Otsuka et al., 2021). TIDs/AGWs are observed by the SuperDARN radars in slant range of the backscattered power and, on occasion, Doppler velocity and spectral width parameters, typically between 600 and 1200 km downrange. TIDs can propagate horizontally, obliquely, and vertically in the ionosphere (Hocke et al., 1996; Tsugawa et al., 2004). Their characteristics such as phase velocity (v), wavelength (λ), period (T), and propagation direction may be estimated (He et al., 2004; Crowley & Rodrigues, 2012; Valladares & Hei, 2012; Grocott et al., 2013). TIDs are mainly grouped as: medium scale TIDs (MSTIDs) (Francis, 1974; Hernández-Pajares et al., 2006; Chou et al., 2017) or large scale TIDs (LSTIDs), based on their characteristics (Tsugawa et al., 2004). MSTIDs have v between 100 and 300 m/s, λ of several 100s km, and T between 15 min and 1 hr (Hocke et al., 1996). LSTIDs have v between 400 and 1000 m/s, $\lambda > 1000$ km, and T between 30 min and 3 hrs (Hocke et al., 1996; Tsugawa et al., 2004).

MSTIDs may occur during the local day, night and in the morning depending on the generating mechanism. Daytime, nighttime, and dusk MSTIDs are associated with the AGWs, Perkins instability and gravity waves generated by the solar terminator (Kotake et al., 2007), respectively. Auroral precipitation and/or periodic polar cap flow may contribute to the generation of MSTIDs. Daytime MSTIDs generated in the auroral region are due to Joule heating and/or Lorentz force (Ishida et al., 2008). F-region MSTIDs were found to have effects on SuperDARN E-region NREs (Hiyadutuje et al., 2022).

A recent study by Hiyadutuje et al. (2022) presented three events where F-region TIDs partially modulated the E-region NREs caused by the GDI. They showed that the TIDs may affect NREs (caused by GDI) via the polarization electric field mapped along the magnetic field lines from F- to E-region at high latitudes. Ivarsen et al. (2023) observed small-scale high-latitude density irregularities between the E- and F-regions, where certain turbulent properties appear to be identical in the two altitude regions. The GDI mechanism responsible for the NREs occurs when there is a density gradient and the electric field in a direction favorable to trigger the GDI (St.-Maurice & Nishitani, 2020; Hiyadutuje et al., 2022). In this study, we present five case studies that show a correlation between the passing of TIDs/AGWs and NREs caused by both FBI and GDI. Based on the understanding of the three cases discussed in Hiyadutuje et al. (2022) and five events presented in this study, we extended the investigation to perform a long term (2010 - 2019) survey of simultaneous occurrence of TIDs and NREs as observed by the Zhongshan HF radar. In the absence of studies linking the effects of MSTIDs on the NREs caused by the FBI, and the non-existence of a long-term study linking these phenomena, the statistical study seeks to establish the quantitative relationship between TIDs and NREs when any of the two instabilities is present.

2 Instrument and data

2.1 Zhongshan SuperDARN HF Radar

The SuperDARN HF radars form a network of 35 coherent scatter radars (Greenwald et al., 1995; Chisham et al., 2007). For most of the radars, each radar's Field Of View (FOV) has 16 narrow beams, where each beam covers an azimuth angle of $\sim 3.24°$ and which makes up roughly 53° azimuth extent. They operate between 8 and 20 MHz and all 16 beams are sounded within a dwell time of 3 or 7 s, every 1 or 2 minutes. Typically each beam has 75 range gates/cells with a pulse length of 300 μs so that one gate has a length of 45 km with the lag to the first range gate of 1200 μs corresponding to a distance of 180 km. Most radars have 1200 cells with a maximum range of about 3555 km (Greenwald et al., 1995; Ogawa et al., 2002), but some radars have more beams and gates.

TIDs and NREs were observed using the Chinese SuperDARN HF radar Zhongshan (69.38°S, 76.38°E geographic coordinates) and (74.9°S, 97.2°E geomagnetic coordinates) in Antarctica. The Zhongshan radar's operating frequency was 10.25 MHz, which means that irregularities of wavelength $\lambda \approx 14.6$ m were observed. Figure 1 shows the FOV of all radars in the southern hemisphere with the Zhongshan HF radar highlighted in red. A set of cells/gates c1, c2 and c3 shows one example amongst many other sets that have been used to estimate the MSTID parameters (He et al., 2004; Hiyadutuje et al., 2022). Its beams are numbered clockwise from beam 0 to 15 as shown on the figure.

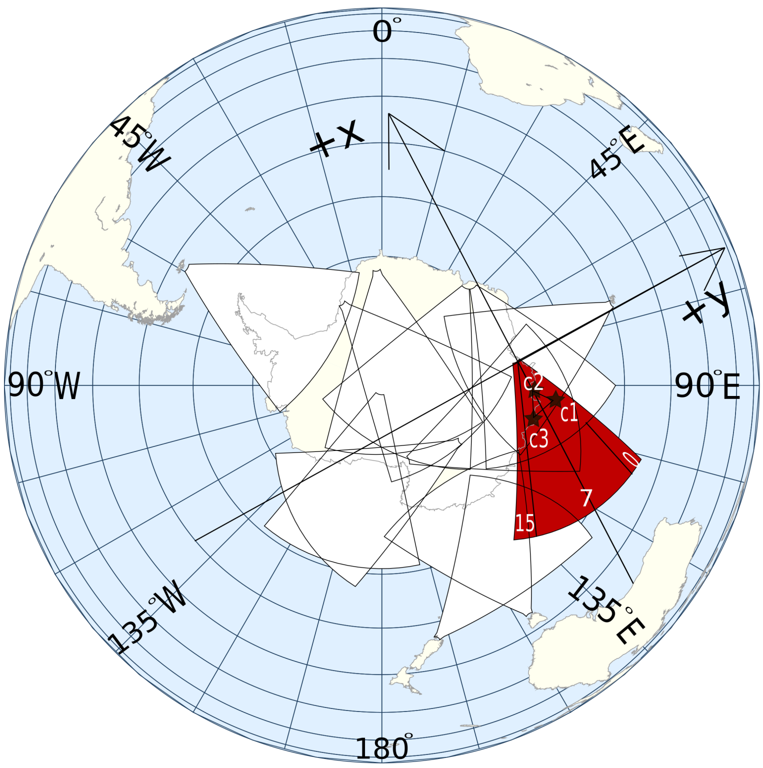

Figure 1. The Zhongshan SuperDARN radar's FOV in red. A set of cells/gates c1, c2 and c3 indicated by three black stars shows an example amongst many other sets that have been used to estimate the MSTID parameters (Hiyadutuje et al., 2022). Beams are numbered clockwise from 0 to 15 and beam 7 is in the middle.

For SuperDARN radars to receive backscatter, the Bragg scatter condition of the effective scatter volume containing the irregularities must be fulfilled. The radar's observations are derived by considering the Doppler frequency shift of the HF signals reflected by the ionospheric irregularities. Their primary parameters are derived from a number of lag Auto Correlation Functions (ACF) between sets of multiple pulses (Milan & Lester, 2001). The backscatter power and spectral width are estimated from a Lorentzian or Gaussian fit to the decorrelation of the ACF, and the line-of-sight Doppler velocity is estimated from a least squares fit to the phase of the complex value of the ACF as a function of lag. In this study, a Lorentzian fit is chosen. The Doppler velocity gives the line-of-sight component of the ionospheric plasma convection where the irregularities are embedded. Doppler velocity is determined from Doppler shifts obtained above 130 km altitude, i.e., in the F-region where ions and electrons both move at nearly the $\mathbf{E}\times\mathbf{B}$ drift. In the E-region, nonlinear effects make the large amplitude waves move at the threshold speed. Only very narrow spectra can have Doppler shifts that correspond to equation (2). At 100 km or thereabout, ψ starts to exceed 0.1 so that even though $V_d \approx (\mathbf{E} \times \mathbf{B})/\mathrm{B}^2$ one should be aware of a Doppler shift slower than the plasma drift even for very narrow spectra. For wider spectra, the Doppler shift is still slow.

The magnetic field conducts the electric field generated from different mechanisms such as the magnetic reconnection and others at the Earth's magnetopause and in magnetotail (Shepherd & Ruohoniemi, 2000) to the ionosphere. The ionospheric plasma drifts in this electric field so that $\mathbf{v} = \mathbf{E}\times\mathbf{B}/B^2$ (Chisham et al., 2008; Haldoupis et al., 2000). The electric field $\mathbf{E}$ is given by $\mathbf{E} = -\nabla\mathbf{\Phi}$, where $\mathbf{\Phi}$ is the polar cap electrostatic potential (Shepherd & Ruohoniemi, 2000). Above 130 km altitude, the plasma (ions and electrons) move at the $\mathbf{E} \times \mathbf{B}$ drift. Between 80 and 120 km, the electrons still follow $\mathbf{E} \times \mathbf{B}$ drift, but not the ions.

For this study, the backscatter power, Doppler velocity, and spectral width data are estimated by fitting the ACF (Ponomarenko et al., 2009), i.e., FITACF Version 2.5 routine through the radar software toolkit (RST) 4.3. Figure 2 shows the Range-Time-Intensity (RTI) plots of backscatter power, Doppler velocity and spectral width of beam 15 of the Zhongshan HF radar for the events considered in this study. The horizontal thick lines in Figure 2 in the far range gates indicate the middle range gate of three gates that are averaged to show the MSTIDs. These three gates were chosen based on the range gates that have few data gaps (by manually inspecting the RTI plots) for each event. We average the data from these three gates to reduce any effect related to data gaps. These TIDs were moving at an altitude of ∼200 - ∼300 km based on the ray tracing at the time when they were visible in the radar's FOV. The generation altitude could be different from ∼200 - ∼300 km. We show in the next section that these TIDs were medium scale. Note that the average of the data from different gates of the same beam does not affect the estimated periods of MSTIDs (He et al., 2004). Horizontal rectangles in the near ranges of the plots indicate the NREs below ∼ 315 km range. Along a particular beam direction, the averaged data of three consecutive range gates representing the MSTIDs are used to compute the Spearman correlation coefficients between MSTIDs and NREs represented by one of four near range gates. Examples of the Spearman correlation coefficient estimation are provided in section 3.

2.2 Data

Figure 2 (A) shows ionospheric backscatter of beam 15 of the first event illustrating the MSTIDs with forward slopes on 04 October 2011 between 07:00 and 12:00 UT. The forward slopes indicate that MSTIDs were moving away from the radar. The top sub-panel of Figure 2 (A) shows the backscatter power in the range 0 - ∼70 dB, where very strong echoes of around ∼70 dB are observed in the near range gates between 07:00 and 09:00 UT. The middle sub-panel of Figure 2 (A) shows the Doppler velocity. For most of the time it was negative to indicate that the ionospheric plasma was moving away from the radar. In the near range gates, within the second, third and fourth gates, from 07:00

and 10:45 UT there are echoes moving away from the radar with Doppler velocity $> \sim 400$ m/s. The first gate shows that the magnitude of the ionospheric plasma velocity projected along beam 15 was sometimes $< \sim 200$ m/s in the direction away from the radar. The bottom sub-panel shows the spectral width in the range between 0 and ~ 180 m/s.

Figure 2 (B) shows the second event where the MSTIDs were again moving away from the radar in the far range gates and NREs in the near range gates on 03 January 2012 between 10:00 and 14:30 UT. All backscatter received by gates 0 - 45 are ionospheric, but some of the backscatter received by gates above 45 are ground/sea scatter (GS). The GS is clearly seen in the middle and bottom sub-panels where the Doppler velocity in grey is ~ 0 m/s and the spectral width in blue is $< \sim 20$ m/s. The top panel shows the backscatter power between 0 and 40 dB. The second sub-panel shows the Doppler velocity also with the ionospheric plasma moving away from the radar with magnitude in the range between ~ 100 and ~ 1000 m/s. Most of the NREs were moving at 400 - 500 m/s. The spectral width was between 0 and $\sim$ 150 m/s.

Figure 2 (C) shows the MSTIDs with backward slopes indicating that MSTIDs were moving toward the radar. It also shows the NREs of the same beam 15 on 29 February 2012 between 00:00 and 05:00 UT. The top sub-plot shows the ionospheric backscatter (below gates 30) and ground backscatter (between gate 30 and 40 from 00:00 to 02:00 UT) power between 0 and ~ 40 dB. The second sub-panel shows that the Doppler velocity of the ionospheric plasma projected along beam 15 was between 0 and 800 m/s toward the radar. We focus on the NREs in the rectangle block, and we see that there was a time where the velocity was below ~ 200 m/s and $> \sim 400$ m/s. The bottom sub-panel shows that the spectral width was between ~ 90 and ~ 250 m/s for most of the time, but there are also some cases where the width was below $\sim$ 90 m/s during this time.

Figure 2 (D) shows the MSTIDs also moving toward the radar and NREs of the beam 15. The top sub-panel indicates that the ionospheric backscatter (below gate 40) and ground backscatter (between gate 40 and 60) power is between 0 and ~ 30 dB. Very strong echoes of around 30 dB appear mostly in the near range gates. The Doppler velocity shown by its middle sub-panel was moving away and toward the radar when looking into different gates in the near range. The magnitude of the velocity was between 0 and $\sim$ 1300 m/s. The highest velocity is observed in the far range gates. The near range gates show that most line-of-sight velocities were below ~ 300 m/s, but sometimes they were between $\sim$ 300 and ~ 500 m/s.

The last event shown in Figure 2 (E) shows the MSTIDs moving away from the radar and NREs both received by beam 15. The top sub-panel shows the ionospheric backscatter power with the magnitude between 0 and ~ 40 dB. Most of the strongest echoes are observed in MSTIDs signatures. The middle sub-panel shows the Doppler velocity of the ionospheric plasma moving away from the radar with a magnitude between 0 and ~ 1000 m/s. The echoes with high velocity were observed in the MSTIDs signature. The NREs had a velocity between ~ 375 and ~ 500 m/s. The bottom sub-panel shows that the spectral width was between 0 and ~ 60 m/s, but for very few cases, the magnitude of the spectral width was $> \sim 100$ m/s.

We rename the events on 04 October 2011, 03 January 2012, 29 February 2012, 28 March 2012, and 16 December 2012 as ZA, ZB, ZC, ZD, and ZE, respectively. The disturbance storm time (Dst), auroral electrojet (AE) and Kp indices are used to investigate the magnetic conditions during the occurrence of the MSTIDs-NREs events. For ZA, ZB, ZC, ZD, and ZE minimum Dst, maximum AE and Kp were -22, -35, -35, -56, and -16 nT, 479, 514, 414, 709, and 445 nT, and 1^{-} - 1, 1^{-} - 1^{+}, 3^{-} - 3^{+}, 4^{+} - 5^{-}, and 2^{-} - 2^{+}, respectively. The AE, Dst, SYM, ASY and Kp indices show that substorms took place during all events, and there were minor/weak storms during the ZB - ZD events (Loewe & Prölss, 1997). A substorm onset is identified when the ASY-D or ASY-H index is > 20 nT within 30 min and AE index is > 300 nT within 10 min (Iyemori & Rao, 1996). See some plots showing the evidence of storms and substorms in the supporting document, section II.

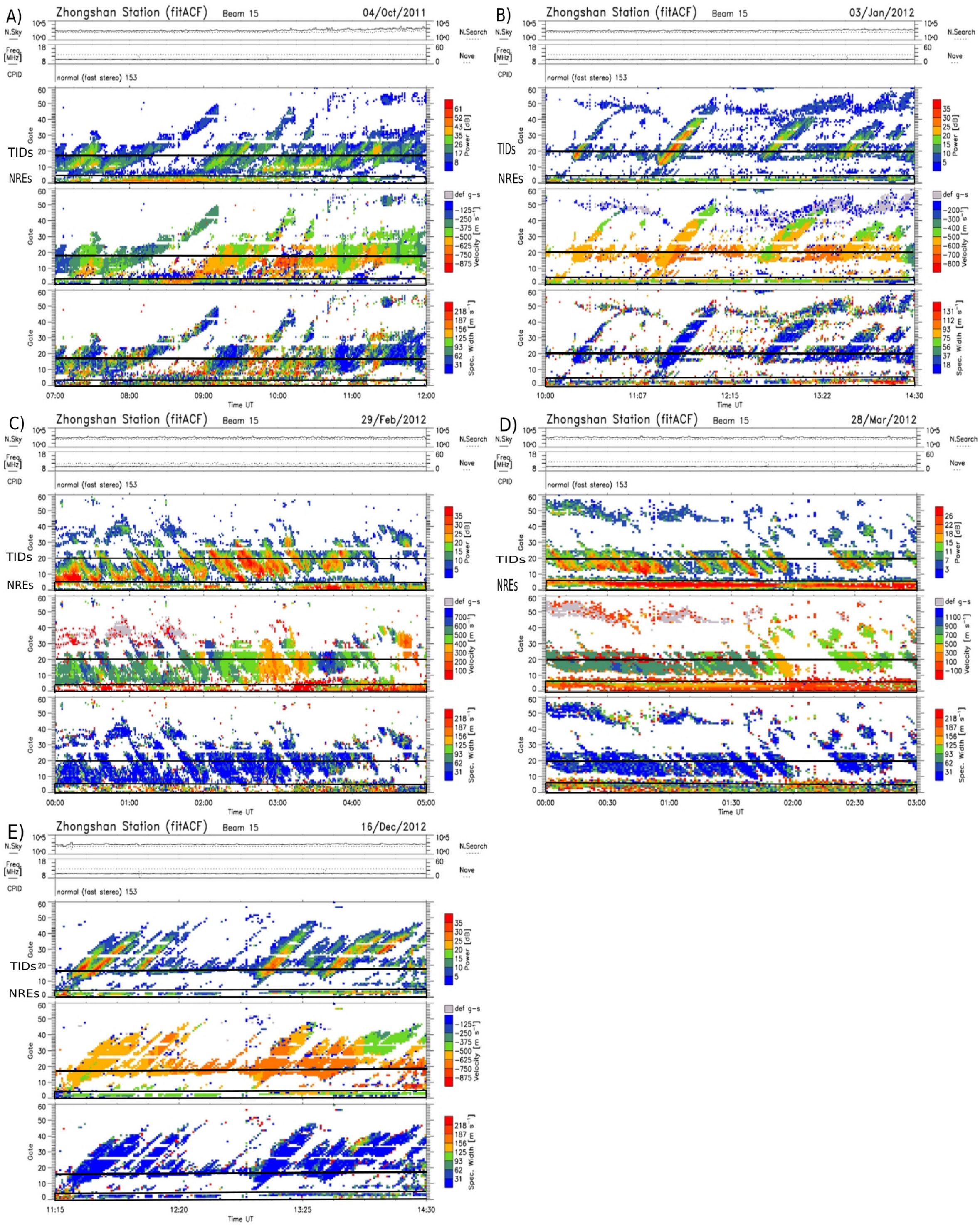

Figure 2. Range-Time-Intensity plots of TIDs and NREs backscatter power, Doppler velocity and spectral width of beam 15 of the Zhongshan HF radar for (A) 07:00 - 12:00 UT on 04 October 2011, (B) 10:00 - 14:30 UT on 03 January 2012, (C) 00:00 - 05:00 UT on 29 February 2012, (D) 00:00 - 03:00 UT on 28 March 2012, and (E) 11:15 - 14:30 UT on 16 December 2012. The selected gates for TIDs to estimate the Spearman correlation coefficients are shown by the horizontal black lines while the NREs are in the rectangles of each figure.

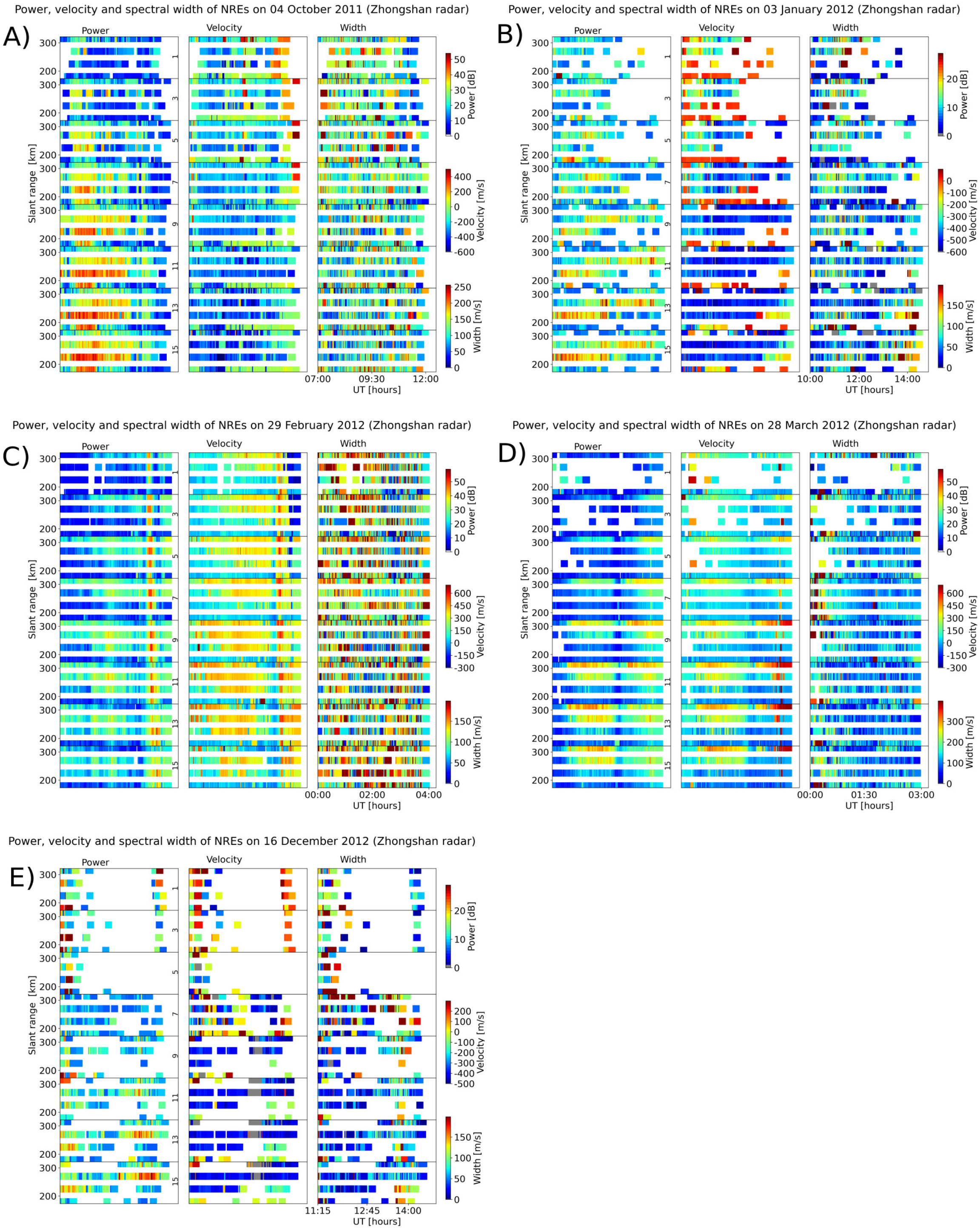

Figure 3. NREs backscatter power, Doppler velocity and spectral width of odd beam numbers of the Zhongshan HF radar from: (A) 07:00 - 12:00 UT on 04 October 2011, (B) 10:00 - 14:30 UT on 03 January 2012, (C) 00:00 - 04:00 UT on 29 February 2012, (D) 00:00 - 03:00 UT on 28 March 2012, and (E) 11:15 - 14:30 UT on 16 December 2012. Gate 0, 1, 2, and 3 is located at 180, 225, 270, and 315 km slant range, respectively.

Figure 3 illustrates the NREs of the odd beam numbers for ZA, ZB, ZC, ZD, and ZE in five panels. We show the plots of the odd beam numbers only. The results are not different from those of even beam numbers. Beam 1 starts at the top while beam 15 is at the bottom of each panel. There are sub-panels showing the backscatter power (left), Doppler velocity (middle), and spectral width (right) in each panel of the figure. Starting from the ZA event in Figure 3 (A), there is an increase of the backscatter power moving across the radar's FOV. This increase is clearly seen from beam 1 where it lasted for a few minutes to beam 15 where the increase in backscatter lasted for almost four hours. We note that in these beams, some gates received backscatter power of order $\sim$60 dB. The middle sub-panel shows the Doppler velocity in the range between -800 m/s and 500 m/s. This velocity is found in all beams, but the bottom beams (15, 13, 11, and 9) show that these high Doppler velocities lasted for longer (from 03:30 to 04:00 UT) compared to the beams at the top (7, 5, 3, and 1), where the high velocity lasted between 03:30 and 04:40 UT. By visual inspection, we can say that the echoes with high velocity correspond to the strong backscatter power on the left-hand side sub-panel. The right-hand side sub-panel shows the spectral width, whereby in most of the beams it was less than 200 m/s.

Figure 3 (B) shows the next event, ZB. This event has a lot of data gaps, especially in beams 1 - 5. The enhancement of the backscatter power (left-hand side) is mostly seen for a long time in the second and third gates, i.e., at 225 and 270 km ranges of beams 9 - 15. However, the enhancement is also seen in the other beams for a short time depending on the considered range gate. The middle side sub-panel shows the Doppler velocity in the range between $\sim$-600 to $\sim$100 m/s. Most of the velocities were between $\sim$-600 and $\sim$-400 m/s (indicated by the blue colour). Again, the spectral width was less than $\sim$200 m/s.

The first sub-panel of Figure 3 (C) (the left-hand side) shows the backscatter power during the event ZC. From 00:00 to 03:00 UT there is enhancement of power in gates 2 and 3 of beams 1 - 7. Beams 9 - 13 show the enhancement of backscatter power in three gates, i.e., 1 - 3. For beam 15, the power enhancement is seen in its gates 1 - 2. From around 00:00 to 04:00 UT, there is a sharp backscatter enhancement in all beams reaching $\sim$60 dB. This sharp enhancement is also seen in the Doppler velocity (middle sub-panel), where the maximum velocity reached $\sim$750 m/s. There is an increase of the Doppler velocity that moves across the beams of Zhongshan HF radar before 03:00 UT. For most of the cases, the spectral width was $< \sim$200 m/s, but there were some occasional cases where the width was $> \sim$300 m/s.

Figure 3 (D) shows the fourth event (ZD) between 00:00 and 03:00 UT. The left-hand sub-panel shows that the backscatter power enhancement was moving across the near range FOV of the radar from beam 15 toward beam 1. The power increase $> \sim$20 dB is seen in the second (225 km), third (270 km) and fourth (315 km) gates of beams 15, 13, and 11. The same power of $> \sim$20 dB were also observed by the third and fourth gates of beams 9, 7, and 5. Also the fourth gate of beam 3 received the backscatter power $> \sim$20 dB between 02:00 and 03:00 UT. The Doppler velocity was between -300 and 800 m/s. The positive velocity (green, yellow and red colour pattern) is observed in the gates and beams where the backscatter enhancement is observed at exactly the same time. The Doppler velocity is negative (blue) at the time and gates where the backscatter power is less than $\sim$20 dB. The left-hand side sub-panel shows the spectral width that is wider ($> \sim$200 m/s) where the backscatter is enhanced and it is narrow ($< \sim$100 m/s) where the backscatter is strong.

Event ZE is shown in Figure 3 (E). From the figure's bottom left-hand side sub-panel, beams 15, 13, 11, and 9 had enhanced backscatter power $> \sim$20 dB within their gates 1 (225 km range), 2 (270 km range), and 3 (315 km range). Beam 7 shows that most of the backscatter power was less than $\sim$20 dB. Beams 5, 3, and 1 have some data points showing the backscatter of less than $\sim$20 dB for most of the time between around 11:15 and 12:00 UT. The Doppler velocity varying between $\sim$-500 and $\sim$300 m/s is shown in the middle sub-panel. The velocity is high (between $\sim$-500 and $\sim$-400 m/s) and low

(∼-300 and ∼300 m/s) where the backscatter is strong (> ∼15 dB) and weak (< ∼15 dB), respectively. As we have seen from the other events, the spectral width presented in the right-hand side was narrow (< ∼100 m/s)/wide (> ∼100 m/s) where the magnitude of the Doppler velocity is high/low, respectively. Narrow spectra indicate that weak turbulence might have taken place and if the aspect angle was large in those cases, it could just be that the modes were observed in their decaying stage.

For all beams in all events, for most of the time for gate 0 (180 km range), the backscatter power, Doppler velocity and spectral width is always < ∼20 dB, < ∼300 m/s, and < ∼200 m/s, respectively. Other near range gates (1 - 3) show that the backscatter power, Doppler velocity and spectral width was > ∼20 dB, > ∼300 m/s and < ∼100 m/s, respectively. The SuperDARN data initially have a time resolution of 2 min, sometimes with data gaps. For further analysis a third-degree polynomial fitting is used to populate the data gaps (Van Camp & Vauterin, 2005; Kaminskyi et al., 2018).

The magnitude of the Doppler velocity ∼400 m/s is an indication that FBI was also involved in the generation of the NREs. Previously, St.-Maurice and Nishitani (2020) suggested that in order to get the FBI-NREs, the electric field has to be of the order > ∼40 mV/m. To verify this condition, we plotted the electric field derived from the SuperDARN HF radar network (Ruohoniemi & Baker, 1998; Shepherd & Ruohoniemi, 2000) and found that sometimes the electric field was indeed greater than 40 mV/m.

Figure 4 shows the electric field (**E**) above two different locations with geomagnetic coordinates (-77.0°, 104.0°, dashed blue lines) (referred to as the near range) and (-80.0°, 128.0°, dashed green lines) taken as the far ranges. It also shows the Doppler velocity of NREs (red) received by range gate 0 of beam 15 (vel015) at (-76.2°, 101.1°) and (black) received by range gate 2 of beam 15 (vel215) at (-76.9°, 104.2°) of the Zhongshan HF radar for the events ZA (panel A), ZB (panel B), ZC (panel C), ZD (panel D), and ZE (panel E). Panel (A) shows the electric field and Doppler velocity of the event ZA. Most of the time the total **E** above the near range (blue) was between ∼20 and ∼38 mV/m, and sometimes reaching ∼40 mV/m between 11:00 and 12:00 UT. The Doppler velocity fluctuation varied between ∼-600 and ∼200 m/s for range gate 0 (red) and ∼-750 and ∼0 m/s for range gate 2 (black). Most of the time the velocity of range gate 0 was fluctuating around ∼-200 and ∼200 m/s. Panel (B) shows the electric field and backscatter power of the event ZB. Above the near range (blue), the electric field **E** was mostly < ∼30 mV/m, but at the location above the far range (green) **E** was > ∼30 mV/m and sometimes reaching 40 mV/m at around 12:15 UT. The Doppler velocity for range gate 0 (red) was fluctuating between ∼-500 and ∼0 m/s between 10:00 and 11:00 UT. There were some data gaps for the rest of the time of this event. The black line shows that the Doppler velocity derived from range gate 2 was fluctuating between ∼-600 and ∼-400 m/s, but sometimes reaching above ∼-200 m/s. Panel (C) shows the electric field fluctuation and Doppler velocity of the event ZC. Above the near range (blue) **E** was fluctuating between ∼10 and ∼30 mV/m. The **E** above the far range (green) was between ∼25 and ∼50 mV/m. From 00:00 to around 03:30, the velocity of range gate 0 (red) in most cases was between ∼-100 and ∼60 m/s but the velocity of range gate 2 (black) shows an increasing trend from around ∼60 to ∼540 m/s. Panel (D) of the figure shows the electric field and Doppler velocity for the event ZD. Above the near range (blue) **E** was between 0 and ∼30 mV/m. The **E** above the far range (green) had a decreasing fluctuating trend from ∼70 to ∼40 mV/m between 00:00 and 01:40 UT. From 01:40 to 02:20 UT, the electric field reduced to ∼10 mV/m and then increased again to ∼50 mV/m at around 03:00 UT. Similar to the velocities from the events above, v215 (black) is generally greater than v015 (red). Panel (E) shows the electric field and Doppler velocity of the event ZE. The **E** above the near range (blue) was fluctuating between ∼10 and ∼30 mV/m. An increasing fluctuation from ∼20 to ∼ 40 mV/m was observed above the far range (green). The Doppler velocity from gate 0 (red) was between ∼-110 and ∼120 m/s, but generally there was a very big data gap. Velocity of range gate 2 (black) as usual is higher than the velocity of range gate 0 (red). It was fluctuating between ∼-570 and

$\sim$-340 m/s. For all these five cases, the electric field was stronger above the far range (green) than the electric field above the near range (blue) of beam 15 of the radar.

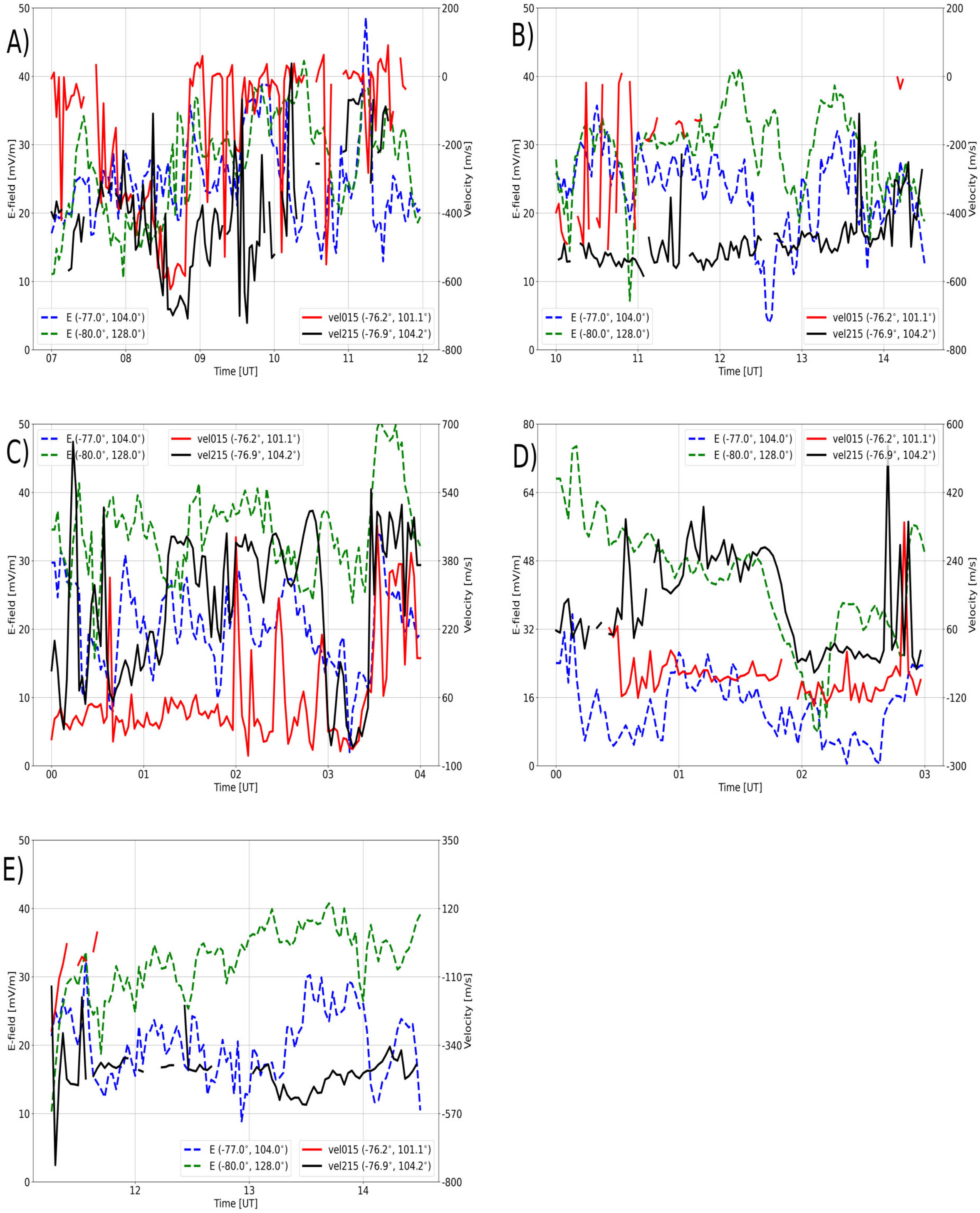

Figure 4. Total electric field (E) and NREs Doppler velocity of range gates 0 (vel015 at -76.2°, 101.1°) and 2 (vel215 at -76.9°, 104.2°) of beam 15 of the Zhongshan HF radar on 04 October 2011 (07:00 - 12:00 UT) (panel A), 03 January 2012 (10:00 - 14:30 UT) (panel B), 29 February 2012 (00:00 - 04:00 UT) (panel C), 28 March 2012 (00:00 - 03:00 UT) (panel D), and 16 December 2012 (11:15 - 14:30 UT) (panel E). Electric field at (-77.0°, 104.2°) in dashed blue and (-80.0°, 128.0°) dashed green corresponds to the geomagnetic location of near range gate 2 (-76.9°, 104.2°) and far range gate 19 (-80.6°, 128.6°) of beam 15, respectively.

A strong electric field in gate 2 does not necessarily mean a large Doppler shift in the same gate. There can be more than one reason for this. one is a matter of direction: the look direction might be well away from the $\mathbf{E} \times \mathbf{B}$ drift direction. Another reason is the refraction: whenever range gate comes from the upper altitudes, the chances to catch a large Doppler shift increase. We can see that the Doppler shift in gate 0 rarely becomes large and the data is more uncertain. It confirms the fact that range gate 0 has data from lower altitudes and larger aspect angles, both of which trigger smaller Doppler shift, irrespective of the ambient electric field strength.

3 Method and results

3.1 Characteristics of MSTIDs

The Fast Fourier Transform (FFT) cross-spectral analysis algorithm developed by He et al. (2004) was used to obtain the TID characteristics. We assume that MSTIDs travel in the x-y plane with x axis passing through the middle beam (beam 7) (see Figure 1). Multiple sets of 3 cells/gates (see Figure 1) from different beams of the Zhongshan HF radar are used to estimate the wavenumber along x (k_x) and y (k_y) directions. The process is repeated for all cells that recorded the MSTIDs and the dominant component of wavenumbers (k_x) and (k_y) are selected. The resultant wavenumber k is estimated (He et al., 2004):

$$k = \sqrt{k_x^2 + k_y^2}. \tag{6}$$

From k_x and k_y, we estimated the azimuth angle using:

$$Az = \tan\left(\frac{k_x}{k_y}\right). \tag{7}$$

The geographic azimuth angle is obtained by considering the boresight direction of the Zhongshan HF radar, which is 72.5°. We estimate the MSTIDs periods (T) using FFT package from the scipy module in python and the period for each event. The wavelength λ is estimated using:

$$\lambda = \frac{2\pi}{k}. \tag{8}$$

We estimate the phase velocity v using:

$$v = \frac{\lambda}{T}. \tag{9}$$

Finally, we estimate the TID vertical oscillation S using (Francis, 1974; Hiyadutuje et al., 2022):

$$S = \frac{v}{\omega}. \tag{10}$$

Table 1 shows the MSTIDs characteristics for all five events. Periods, propagation azimuth angles, wavelengths, phase velocities, and S were 32 - 60 min, 105.2 - 285.1°, 385.1 - 629.2 km, and 107.2 - 200.6 m/s, 61.3 - 100.1 km respectively. Indeed, these characteristics indicate that we observed MSTIDs. These characteristics are in line with other studies. Their periods, wavelengths, and velocities were between ∼20 and ∼ 80 min, ∼100 and ∼800 km, ∼40 and 400 m/s, respectively (Samson et al., 1990; Bristow & Greenwald, 1997; Hall et al., 1999; He et al., 2004; Ishida et al., 2008; Ogawa et al., 2009; Suzuki et al., 2009; Vlasov et al., 2011; Grocott et al., 2013; Frissell et al., 2014; Liu et al., 2019).

3.2 Correlation between MSTIDs and NREs

To find the relationship between MSTIDs and NREs in this study, we compute the crosss correlation between their respective backscatter power. For MSTIDs dataset, we

Table 1. The MSTIDs periods, wavenumber, geographic azimuth angle, wavelength and phase velocity

Parameters	04/10/2011	03/01/2012	29/02/2012	28/03/2012	16/12/2012
Period (min)	50	60	40	60	32
kx (/m)	10.0×10^{-6}	5.4×10^{-6}	11.0×10^{-6}	14.7×10^{-6}	13.8×10^{-6}
ky (/m)	6.5×10^{-6}	8.4×10^{-6}	6.9×10^{-6}	7.0×10^{-6}	8.7×10^{-6}
k (/m)	11.9×10^{-6}	10.0×10^{-6}	13.0×10^{-6}	16.3×10^{-6}	16.3×10^{-6}
Az (°)	106.0	148.3	285.1	278.5	105.2
λ (km)	526.8	629.2	483.9	385.9	385.1
v (m/s)	175.6	174.8	201.6	107.2	200.6
S (km)	83.8	100.1	77.0	61.4	61.3

Table 2. The Cross Correlation Coefficient, time lag, Spearman correlation coefficient, percentage of the Spearman correlation coefficient, and p-values between NREs (GDI-FBI) and MSTIDs

Event	NREs gate	MSTIDs gates	Correlation	Time lag (min)	SCC	percentage	p-value
ZA	0	16 - 18	-0.570	25	-0.474	∼22.5%	0.000
ZA	1	16 - 18	-0.590	25	-0.413	∼17.1%	0.000
ZB	0	19 - 21	-0.225	20	-0.240	∼5.8%	0.008
ZB	3	19 - 21	-0.385	20	-0.335	∼11.2%	0.000
ZC	0	19 - 21	0.260	20	0.334	∼11.1%	0.000
ZC	3	19 - 21	-0.370	20	-0.353	∼12.5%	0.000
ZD	2	19 - 21	-0.350	20	-0.307	∼9.4%	0.028
ZE	2	15 - 17	0.480	15	0.475	∼22.6%	0.000

use the average backscatter power in dB of three far range cells/gates, i.e., the power received when MSTIDs pass over those 3 cells, to reduce the data gap effects in each gate. For NREs dataset, we use a single near range cell/gate of the same beam of the Zhongshan radar.

We calculate the Spearman correlation coefficient between MSTIDs and NREs (Zou et al., 2003; Wilks, 2011; Rauf et al., 2019). The Spearman correlation coefficient is the Pearson correlation calculated by considering the rank of the data, hence the Spearman correlation coefficient is not affected by the outliers (Zou et al., 2003; Wilks, 2011; Rauf et al., 2019). The Pearson correlation coefficient is given by $(Cov_{(NREs,TIDs)})/(S_{NREs}S_{TIDs})$, where Cov and S represent covariance and standard deviation, respectively. Apart from the Spearman correlation coefficient, the Linear Regression Correlation Coefficient (LRCC) was also computed. We compute the F-statistics (P-values) to test the statistical significance of the correlation coefficient. We reject the null hypothesis when P-value for the correlation coefficient is less than 5% ($\alpha < 5\%$ is the significance level). In this case, we consider this correlation coefficient to be statistically significant with a 95% confidence level (Rauf et al., 2019; Ware et al., 2019).

Correlations in the range of [±0.00 ±0.19], [±0.20 ±0.39], [±0.40 ±0.59],[±0.60 ±0.79],[±0.80 ±1.00] are very weak, weak, moderate, strong and very strong, respectively (Rauf et al., 2019). To investigate the relationship between MSTIDs and NREs, we use the square of the correlation coefficient. The square of the correlation coefficients in percentage, i.e., [0 3.61], [4 15.21], [16 34.81], [36 62.41], [64 100], respectively indicate the range of percentages by which the parameters of one variable could be statistically explained by the parameters of the other (Rauf et al., 2019).

3.2.1 MSTIDs effects on the FAIR and HAIR (NREs) echoes

Assuming, the elevation angle of the returned signals to be ∼30°, we estimated the virtual height (Ponomarenko et al., 2015) of gates 0 - 3 to be ∼93 - 163 km, respectively. The time shift between the MSTIDs (horizontal black line in Figure 2) and NREs was estimated to be ∼25, ∼20, ∼20, ∼20, and ∼15 min for ZA, ZB, ZC, ZD and ZE, respectively. Adjusting for the time shift first, we performed the Cross Correlation and Spearman correlation coefficient between the backscatter power of NREs and the average backscatter power of three far range gates for MSTIDs. Figure 5 shows scatter plots estimated based on the rank of TIDs backscatter power and NREs backscatter power. Inserted in each figure are the Spearman correlation coefficient, LRCC, and p-values on 04 October 2011 between 07:00 and 12:00 UT (event ZA) for gate 0 (NREs) and gates 16 - 18 (MSTIDs) (A) and for gate 1 (NREs) and gates 16 - 18 (MSTIDs) (B) of beam 15 of the Zhongshan radar. The p-values of 0.000 - 0.050 (see Figure 5 and Table 2) indicate that the correlation coefficients were statistically significant with a 95% confidence level. The Spearman correlation coefficient values of -0.474 and -0.413 in (A) and (B) indicate that ∼22.5% and ∼17.1% of the NREs power can be statistically explained by the variation of the TIDs backscatter power. In (A) and (B) NREs power was received by gates 0 and 1 (both from beam 15) while TIDs backscatter power came from gates 16 - 18, respectively. Additional figures are found in the supporting document (section I). Table 2 shows the cross correlation coefficient, time lag, Spearman correlation coefficients, percentage derived from the Spearman correlation coefficients and p-values. It shows both negative and positive Spearman correlation coefficients, but in most cases, the Spearman correlation coefficient was negative.

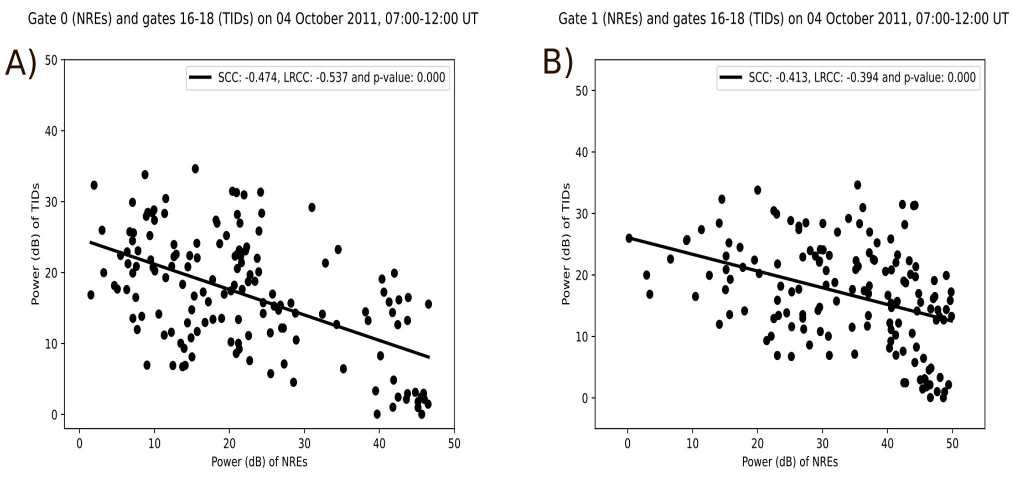

Figure 5. The Spearman correlation coefficients, LRCC, and p-values of range gate 0 (A) and gate (1) (B) backscatter power (NREs) and range gates 16 - 18 backscatter power (MSTIDs) at 07:00 - 12:00 UT on 04 October 2011 (event ZA).

These values agree well with the recent study presented by Hiyadutuje et al. (2022), where they found that there was a partial modulation of NREs backscatter power (caused by GDI) by the MSTID polarization electric field of about ∼10%. Sun et al. (2015) and Otsuka et al. (2009) found the air glow intensity perturbation of 25% and 30% were due to the MSTIDs polarization electric field. In addition to three events reported in Hiyadutuje et al. (2022), we have analyzed another five cases where we have found a weak to moderate correlation between MSTIDs and NREs characterized by both GDI and FBI.

The issue that arises from this analysis is the need to understand and establish the occurrence rate of these events on a long term and whether they exhibit some seasonal dependence. We also perform a statistical study of the Spearman correlation coefficients and p-values for all 1074 events between 2010 and 2019. In the next section, we provide more details on this. Figures 1 - 6 of the supporting document are similar to Figure 5 but for the different events.

3.3 Statistical analysis of MSTID-NRE events

3.3.1 Occurrence of MSTID-NRE events

NREs appear almost all the time (Ponomarenko et al., 2016), but MSTIDs occur occasionally depending on the topographic conditions and other sources of energy in the ionosphere (Hocke et al., 1996; Tsugawa et al., 2007). We investigated the simultaneous occurrence of MSTID-NRE events. All together we found 1074 events observed by the Zhongshan HF radar from 2010 to 2019. Only events that lasted for at least an hour were analyzed since the NREs in the current study have at least a duration of an hour (Ponomarenko et al., 2016; St.-Maurice & Nishitani, 2020; Hiyadutuje et al., 2022). The summary of the 1074 events recorded between 2010 - 2019 is presented in Figure 6. Figure 6 (A) shows the number of events grouped based on their duration in hourly bins. About 61.4% of the events lasted between 4 and 8 hours. About 12.0% lasted for less than 4 hours and ∼26.6% lasted for more than 8 hours.

Figure 6 (B) presents the starting time of each event in UT along the abscissa axis and LT (at the top of the plot). The duration in hourly bins is presented along y-axis. Around 67.6% of events started in the time interval from the afternoon (15:00 LT) to midnight (around 24:00 LT).

Figure 6 (C) shows the distribution of the 1074 events grouped by month from 2010 to 2019. The normalized number of events in each month is estimated by dividing the total number of the events in each month with the total number of events observed between 15:00 and 24:00 UT (509 ≈ 47.4% of all events). This normalization doesn't change the seasonal variability trend of the MSTIDs-NREs events compared to when presented using the total number of events in each month. Each year can be divided into three seasons (Kotake et al., 2007), i.e., summer (November - February), equinoxes (March - April and September - October) and winter (May - August) in the southern hemisphere. Among 1074 events, there are 40.5% events in summer, ∼38.1% during the equinox and ∼21.4% in winter. This figure shows that the majority occurred in summer or equinox with the peak in November while the minority occurred in winter with the low in June.

Figure 6 (D) shows the yearly occurrence number for the joint MSTIDs-NRE events and sunspot numbers. From 2010 to 2013 there were some days by which the radar didn't receive data. The reason of the missing data is not known. The majority of the events (> 89.1%) occurred between 2014 and 2019. During this time the radar did not have many data gaps. From 2014 to 2019 when the solar activity was declining, the MSTIDs-NREs events were increasing. About 73.9% of all events took place during geomagnetic quiet time and about 26.1% occurred during geomagnetic storms.

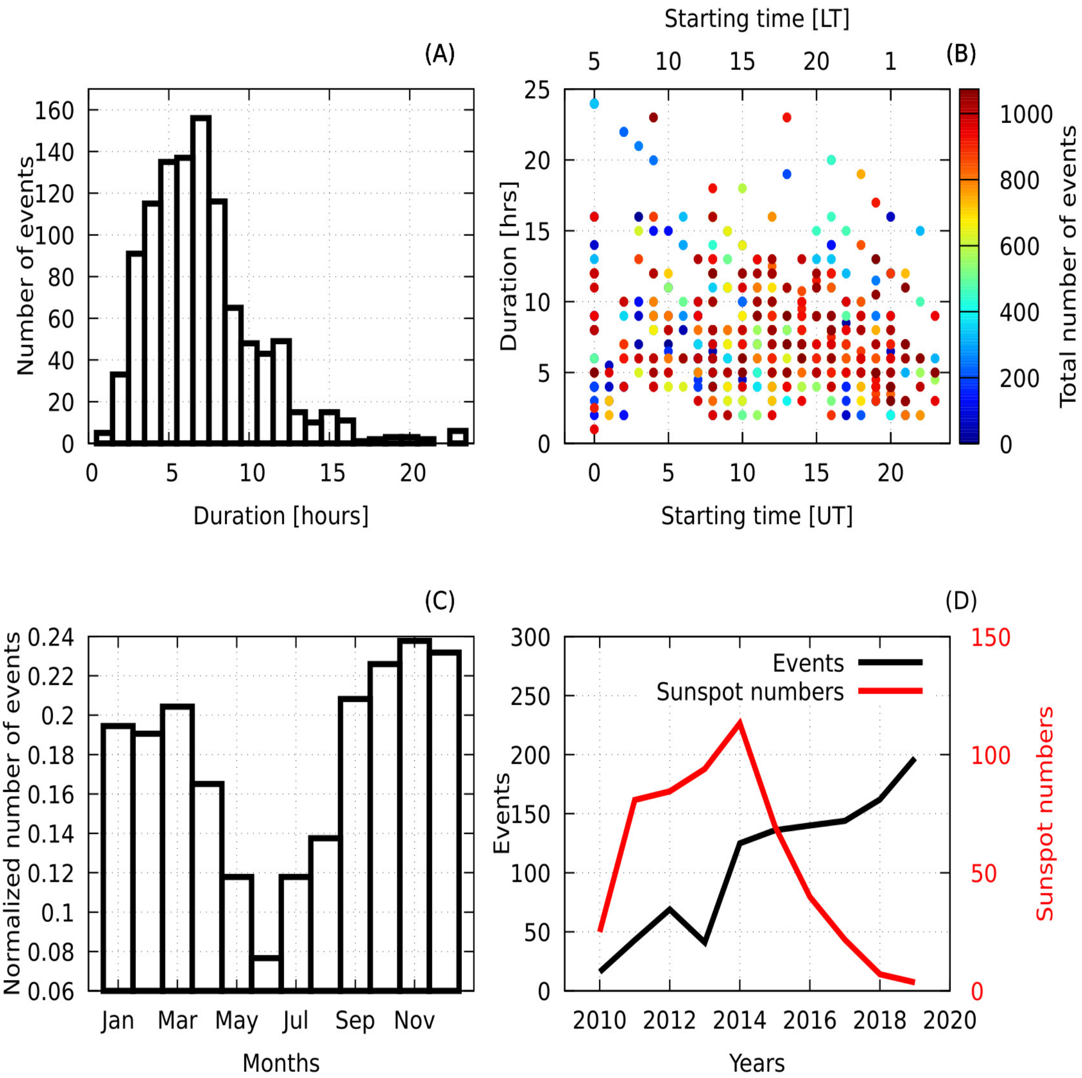

Figure 6. Simultaneous occurrence of MSTIDs and NREs between 2010 and 2019. Panel (A) groups the events based on their duration, panel (B) shows all 1074 events starting time in UT and LT and the duration of each event on the y-axis. Panel (C) shows the normalized number of events from January to December of the 9 years (2010 - 2019). Panel (D) shows the number of events and the mean sunspot number (red) recorded every year.

3.3.2 Statistical analysis of the Spearman correlation coefficient values between MSTIDs and NREs

The Spearman correlation coefficients and p-values are estimated for 1074 events. MSTIDs were observed within the far range gates (average backscatter power of gates 16 - 18) while the NREs observed by the near range gates (backscatter power of each of 4 gates, i.e., 0 - 3). For each event, we obtain 4 values corresponding to the number of near range gates. In total, we found 4296 Spearman correlation coefficients and p-values of which 77.3% had p-value of < 0.005 (accepted) and 23.7% had p-value of > 0.005 (rejected). We then perform the statistics of the accepted 3322 Spearman correlation coefficient values where p-values indicate that there is a correlation between MSTIDs and NREs.

Figure 7 shows the binned the Spearman correlation coefficient values based on the five classes of the correlation (section 3.2). About 71.4%, 17.6%, 4.6%, 3.3%, and 3.1% of the values are in very weak (blue), weak (black), moderate (red), strong (green), and very strong (yellow) correlation category, respectively. The red dashed curve shows a symmetric normal distribution fitting of data where the mean (μ) and standard deviation (σ) were 0.0 and 0.3, respectively. The value of $\mu = 0$ indicates that there are almost equal number of negative and positive Spearman correlation coefficient values.

Those values could be caused by the relative velocity between the E-region NREs and the F-region MSTIDs switching the electric field polarities between the crests and the troughs (Kelley et al., 2023). Either positive or negative polarization electric field is mapped down to the E-region to affect the NREs (Hiyadutuje et al., 2022). Another reason of the negative and positive correlation may be associated with the electrons that are magnetized and ions that are collisional in the E-region creating the ionospheric current or electrojet that is in the opposite and same direction as that of MSTID polarization electric field, respectively. The westward zonal component of convection pattern at lower altitudes of the high latitude southern hemisphere was found to be predominant (Forsythe & Makarevich, 2017). The eastward/westward components of the MSTID polarization electric field would subtract/add to the background electric field to cause the negative/positive correlation, respectively.

The standard deviation σ of all values in all events is $\sim$0.3. Its variance $\sigma^2 = \sim 9\%$ represents the contribution of MSTIDs on NREs because it is derived from the square of the standard deviation of the Spearman correlation coefficient values. This MSTID's contribution to the NRE is in agreement with other previous studies which reported that there could be a polarization electric field of $\sim$10 - $\sim$30% of the background electric field due to the MSTID (Otsuka et al., 2007, 2009; Hiyadutuje et al., 2022).

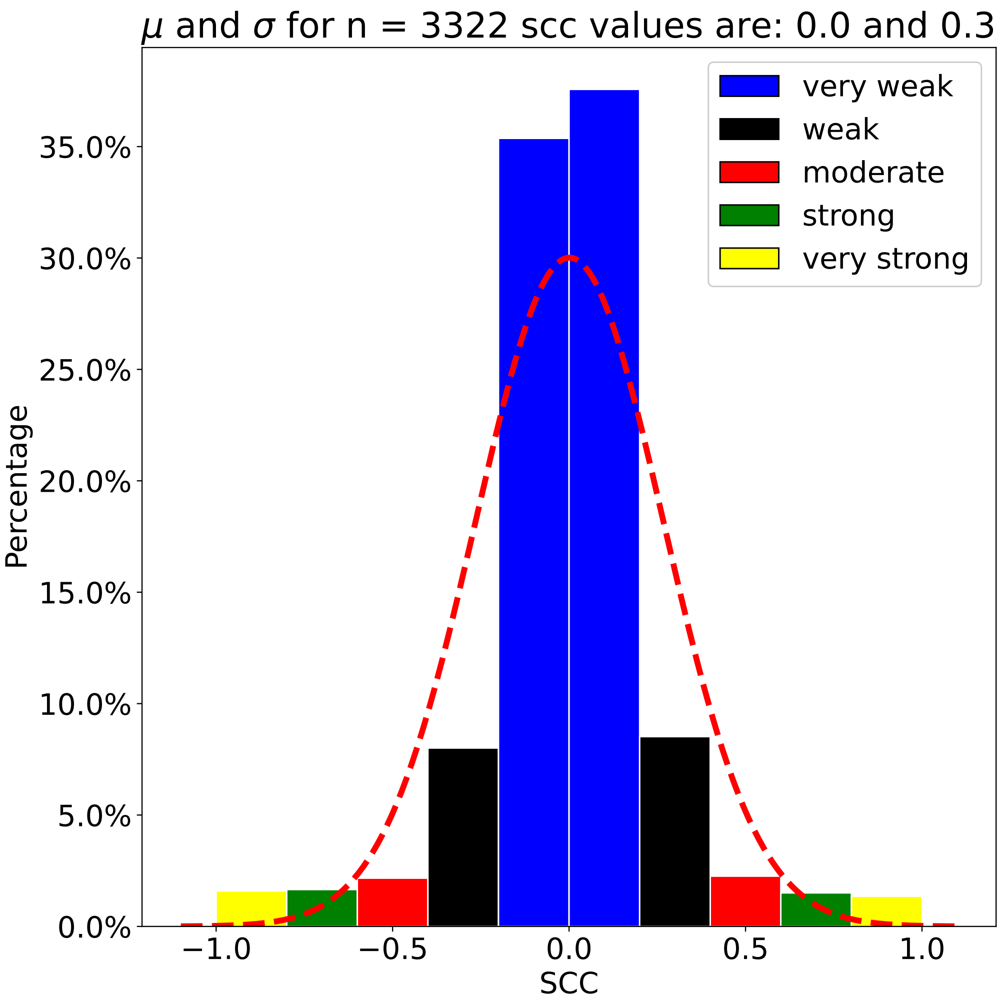

Figure 7. The Spearman correlation coefficient values between MSTIDs (average of backscatter power received by gates 16 - 18) and NREs (gates 0 - 3) of 1074 events for 2010 - 2019.

However, the true cause of these negative and positive Spearman correlation coefficient is beyond the scope of this study and it needs more work.

4 Discussion

In this study, we show that the MSTIDs partially modulate the NREs caused by FBI and GDI. We discuss the findings in this article by considering two ionospheric heights where the MSTIDs can be observed based on the ray tracing plots.

Figures 13 - 17 in the supporting document show the ray tracing plots of beam 15 of the Zhongshan HF radar operating at 10 MHz of the events ZA - ZE. The ray tracing plots show that backscatter is possible from the E-region at ∼100 km altitude or from the F-region at ∼200 - ∼300 km. Without angle of arrival data, we cannot determine the altitude. It is possible that TIDs could travel lower in the E-region close to the NREs altitude, in which case they would be considered as AGWs (Nygrén et al., 2015). Neutral particles dominate in this region and the ion production and loss rates are too fast to allow the propagation of the TID, i.e., compression and rarefaction of electron density is not easily possible (Nygrén et al., 2015). When the ion-neutral collision frequency is greater than kC_s, FAIR echoes are likely to be detected in the near ranges of the radar. St.-Maurice and Nishitani (2020) noted that AGWs may modulate the vertical scale height L_z of GDI which is the generation mechanism of the FAIR echoes. The AGWs would move the plasma up and down through shear or compression (St.-Maurice & Nishitani, 2020). FBI responsible for the HAIR echoes will also be affected by the passing AGWs.

The effects of MSTIDs in the F-region on NREs caused by GDI in E-region were discussed by Hiyadutuje et al. (2022). In this study, the meridional convection electric field and zonal neutral wind were proposed to generate the GDI in the presence of the plasma density gradient. To maintain divergence-free current continuity for the Pedersen current $\mathbf{J}$ in F-region, a periodic horizontal polarization electric field ($\mathbf{E_{pF}} = [\delta\Sigma_p/\Sigma_p](\mathbf{E}+\mathbf{U}\times\mathbf{B})[\mathbf{k}/|\mathbf{k}|]$) takes place within the MSTID wave. Figure 7 of Hiyadutuje et al. (2022) shows the polarization electric field generated by a passing MSTID wave. The Pedersen current is given by $\mathbf{J} = \Sigma_p(\mathbf{E} + \mathbf{U} \times \mathbf{B})$, where Σ_p is the F-region Pedersen conductance, $\mathbf{E}$ is the electric field, $\mathbf{U}$ is the neutral wind and $\mathbf{B}$ is the magnetic field (Haldoupis et al., 2003). For the current study, we estimated the ratios of the Pedersen conductivity perturbation to the background ($\delta\Sigma_p/\Sigma_p$) using an ionospheric conductivity model, height profile (https://wdc.kugi.kyoto-u.ac.jp/ionocond/sigcal/index.html). We use MSTID's constant S of 84, 100, 77, 61, 61 km (see Table 1) for events ZA (10:00 UT), ZB (12:00 UT), ZC (02:00 UT), ZD (02:00 UT), and ZE (12:00 UT), respectively. Based on the ray tracing, we assume that MSTIDs traveled at an altitude of 300 km (ZA, ZC, and ZD) and 240 km (ZB and ZE). For all five events, we found that $\delta\Sigma_p/\Sigma_p$ were 5 - 21%, which are in the same range as the Spearman correlation coefficients of 6 - 23% estimated earlier (see Table 2). The long-term statistical study shows that the mean and standard deviation of the Spearman correlation coefficient values is 0 and 0.3, respectively indicating that the positive and negative Spearman correlation coefficient values where MSTIDs partially affected NREs, i.e., by ∼9%, are almost equal. These values agree well with the previous studies (Otsuka et al., 2007, 2009; Hiyadutuje et al., 2022).

The FBI mechanism strongly depends on the relative drift between the ions and electrons in the E-region of the high-latitudes. Equation (2) defining the plasma oscillation frequency depends on equation (3) which shows that there is directly proportionality between $\mathbf{V}_d$ and $\mathbf{E}$. Equation (4) defining the growth rate of both instabilities show that the FBI growth rate strongly depends on $\mathbf{E}$. The partial modulation of the electric field will cause the FBI echoes, such as HAIR to be partially modulated by the MSTIDs passing overhead in the F-region.

Electric field and Doppler velocity presented in Figure 4 illustrate that range gate 0 is most likely to receive FAIR echoes from around 100 km altitude while range gate 2 is populated by HAIR echoes from around 110 km altitude. For range gate 0, a 40 mV/m E field would be required to observe decaying modes at 400 m/s. An E field of the order of > 20 mV/m (∼30 mV/m as shown in this study) is expected to observe HAIR echoes in gate 2. Gate 1 would be populated by both FAIR and HAIR echoes between 100 and 110 km altitude while range gate 3 is most likely populated by HAIR echoes from around 120 km altitude and above. Note that backscatter power, Doppler velocity and spectral width of range gates 0 - 3 for the five events are presented in Figure 3.

A long term occurrence rate of the MSTIDs-NREs events (mainly depends on the MSTIDs occurrence) is performed and compared with other previous studies. The results in this study agree with those presented by Galushko et al. (2016) using Total Electron Content (TEC) over the Antarctic Peninsula between April 2009 and June 2012. They found that the winter peak of MSTID occurrence was observed at local noon time in winter while the summer peak of the MSTID occurrence took place during nights and mornings. Kotake et al. (2007) used month-hour bin of the MSTID occurrence over the southern Califonia and found that during the equinoxes and winter the occurrence was high in the morning (0600 - 1200 LT). The occurrence was also high during dusk (1700 - 2000 LT) and nighttime (2100 - 0300 LT) in summer.

Nighttime MSTIDs may have been caused by the Perkins instability, which is inversely proportional to the solar activity (Otsuka et al., 2021). The statistics of MSTIDs-NREs occurrence in this study mainly depends on the existence of the MSTIDs in SuperDARN data, i.e., when there were only NREs without MSTIDs, the events were not counted. NREs occur almost all the time depending on different mechanisms such as the meteor trails and turbulence associated with the auroral activity and particle precipitation (Kirkwood & Nilsson, 2000; Ponomarenko et al., 2016). Figure 6 shows that the majority of the events took place during summer and equinox at nighttime. The nighttime peak of the MSTIDs-NREs events during summer and equinox presented in Figure 6 (B) and (C) is explained by the linear growth rate of the Perkins instability (Perkins, 1973; Hamza, 1999) causing the nighttime MSTIDs (Otsuka et al., 2013; Tsuchiya et al., 2019).

The MSTIDs polarization electric field is mapped along the magnetic field lines to modulate NREs. Other studies suggested that the electric field from the Es layer instability in E-region would also be mapped to the F-region to modulate the Perkins instability during the night (Cosgrove, 2007; Atilaw et al., 2021). Our results also agree well with the solar activity dependence of MSTIDs using Global Positioning Satellite (GPS) receivers in Japan by Otsuka et al. (2021). For a period of 22 years observations, they found that the nighttime MSTID activity and occurrence rate increased with the decrease of solar activity which may be explained by the Perkins instability theory. There exists an inverse proportionality relationship between the Perkins instability linear growth rate (γ_P) and the ion-neutral collision frequency (ν_{in}) estimated along the magnetic field and as a function of plasma density (Perkins, 1973). The ν_{in} is directly proportional to the neutral density (n), which increases with the solar activity increase, implying the anticorrelation between γ_P and the solar activity.

The polarization electric field and the height-integrated Pedersen conductivity in F-region (Otsuka et al., 2021) also could be playing a role in the anticorrelation between MSTIDs-NREs and the solar activity. Martinis et al. (2010) pointed that γ_P is inversely proportional to the neutral density. Hazeyama et al. (2022) using the SuperDARN Hokkaido pair of radars found a negative correlation between the nighttime amplitude and the solar EUV 10.7 cm radio flux known as F10.7 index, linking those MSTIDs with the linear growth rate of the Perkins instability. Although, we can't conclude on the findings between 2010 and 2013 due to the unavailability of enough data, we can conclude that from 2014 to 2019 the occurrence rate of MSTIDs-NREs increased when the 24^{th} solar cycle activity was decreasing (see Figure 6 D).

Different instruments were used to investigate the MSTIDs occurrence and found the results that disagree with the current study. Ogawa et al. (1987) used Global Navigation Satellite System (GNSS) satellites and differential-Doppler measurements of the 150 and 400 MHz beacon waves to study MSTIDs at Syowa station. They investigated events between March 1985 and January 1986, where their results agree well with ours for the geomagnetic condition dependence. However, they disagree on seasonal dependence where the majority of MSTIDs occurred during winter (August) and minority in summer (January). The reason for their results were associated with the detectability of total electron content and the seasonal dependence of gravity wave activity in the high-latitude middle atmosphere. There is a threshold value of the ambient electron density ($foF2$) on which the acoustic gravity waves depend on (Ogawa et al., 1987).

Similarly, SuperDARN HF radar echoes depend on the aspect and/or Bragg scatter conditions and the threshold of electron density. There is a threshold value of electron density in F- and E-region required for backscatter echoes (Vickrey & Kelley, 1982; Danskin et al., 2002). In a very dense E-region, conductivity enhancement may slow down or prevent the F-region instabilities (Danskin et al., 2002). Note that Perkins instability (Perkins, 1973) takes place at night when the E-region conductivity is low. Sometimes, signals are absorbed in the D-region or over-refracted to higher altitude and never return to the radar when F-region density is very low of $< 10^{11}$ m^{-3} or very high of $> 4 \times 10^{11}$ m^{-3}, respectively (Danskin et al., 2002). Note that high-energy particle precipitation at night can provide strong conductivity modulations in the E-region (Robinson et al., 2021). HF radars such as SuperDARN, experience a loss of backscatter during geomagnetic storms (Currie et al., 2016). This loss could explain the low number of events between 2010 and 2014 when the sunspot number was increasing. This also means that there is a good sensitivity for these HF radars during quiet time hence the increase number of events between 2014 and 2019.

5 Conclusions

In this paper, the effects of MSTIDs on NREs caused by the FBI and GDI during their near simultaneous occurrence are presented. Five events showing both phenomena are analyzed and discussed. We have also performed a climatology study of simultaneous MSTIDs-NREs occurrence and the statistics of the Spearman correlation coefficients and p-values between 2010 and 2019. Statistically, we have computed:

- the Spearman correlation coefficient values to find a relationship between the MSTIDs and NREs, the correlation coefficients are based on a relationship between the backscatter power in MSTIDS and the backscatter power in NREs,
- the daily and seasonal occurrence of the joint MSTID-NRE events between 2010 and 2019, including their geomagnetic activity condition.

We have computed the Spearman correlation coefficient between the SuperDARN HF radar's backscatter power showing the MSTIDs and NREs driven by the FBI and/or GDI. For the investigated gates of beam 15, we have found a negative and positive correlation between MSTIDs backscatter power and NREs backscatter power based on a long term statistical study of the Spearman correlation coefficient values from the more robust Spearman rank correlation analysis, i.e., $\sim$9% of the NREs backscatter power are due to the MSTIDs. The correlation agrees well with previous studies that MSTIDs may produce a polarization electric field of $\sim$10 - 30% in the ionospheric F-region (Otsuka et al., 2007; Kotake et al., 2007; Suzuki et al., 2009; Otsuka et al., 2009; Hiyadutuje et al., 2022).

Daytime MSTIDs may have been generated by the AGWs, Joule heating and/or Lorentz force while the nighttime MSTIDs can be generated by the electro-dynamical forces such as the Perkins instability as previously discussed by other researchers (Perkins, 1973; Hamza, 1999; Cosgrove, 2007; Otsuka et al., 2021). MSTIDs during dusk were due to the gravity waves caused by the solar terminator (Kotake et al., 2006, 2007). We have chosen two ionospheric heights by which these waves could be traveling in the ionosphere based on the SuperDARN ray tracing tool results. First, at $\sim$100 km altitude, the disturbances may be AGWs and would partially modulate NREs through shear or compression. Second, between $\sim$180 and $\sim$300 km these waves are MSTIDs and would partially modulate NREs via the polarization electric field (Hiyadutuje et al., 2022).

This study also presents the occurrence rate analysis of concurrent MSTIDs and NREs. From inspection of 9 years of data, we show that about 61.4% lasted for 4 - 8 hrs, and 67.6% started in the local night. Most of the events ($\sim$40.5%) took place in summer, followed by $\sim$38.1% in equinoxes while the minimum of $\sim$21.4% took place in winter. We also grouped 1074 events based on the geomagnetic conditions during their occurrence time as either quiet, i.e., $Kp < 3$ or disturbed, i.e., $Kp > 4$ (Galushko et al., 1998). The majority of the events ($\sim$73.9%) took place during geomagnetic quiet condition while $\sim$26.1% took place during geomagnetic storms.

Since the majority of MSTIDs-NREs events took place during the nighttime, quiet time condition, and in summer or equinoxes, the proposed mechanism associated with MSTIDs in most of these events is the Perkins instability (Cosgrove, 2007). Other mechanisms such as gravity waves, solar terminator, auroral precipitation particles and/or periodic polar cap flow would have contributed to the MSTIDs occurrence, through Joule heating and Lorentz forcing. NREs are attributed to the FBI and/or GDI.

From the current study, one should consider the existence of the TID polarization electric field when studying the E-region phenomena such as sporadic E-region and sodium layers involving the electric field in their electrodynamics. There are still other points from this study that need to be addressed in the future. Firstly, the physics behind the negative and positive correlation between MSTIDs and NREs need to be clarified. Secondary, Doppler shift and other SuperDARN radar parameters of the two phenomena could be investigated to understand better the link between MSTIDs and NREs. Lastly, the long-term statistical study of MSTIDs-NREs can be extended to other SuperDARN radars in both hemispheres.

Open Research

The processed SuperDARN data in yyyymmdd.txt format and list of events used for the Zhongshan HF radar in the study are available at Mendeley Data via

https://doi.org/10.17632/9skd2fw4yy.1 or https://data.mendeley.com/preview/9skd2fw4yy with the Creative Commons Attribution 4.0 International (CC BY 4.0) Licence that allows you to share, copy, and modify this dataset (read the licence for more information), note that you may be required to register in order to access the data (Hiyadutuje et al., 2023). SuperDARN data should be acknowledged as indicated in the acknowledgements section of this manuscript and the Principal Investigator(s) PI(s) of the used radar(s) should be concerted before using the data (https://www.unis.no/project/superdarn-radar/). The Zhongshan SuperDARN raw data are available from the BAS SuperDARN data mirror (https://ww w.bas.ac.uk/project/superdarn/#data). Alternatively, the data can be found at https://data.meridianproject.ac.cn/. SuperDARN radar data at Zhongshan station belong to the Chinese Meridian Project (https://data.meridianproject.ac.cn/) and Chinese National Polar Scientific Data Center (https://en.pric.org.cn/). The sunspot numbers data are downloaded from the National Oceanic and Atmospheric Administration (Space Weather Prediction Center) via https://www.sidc.be/silso/datafiles. Magnetic Indices Data were obtained through the Kyoto website: Kp index (https://wdc.kugi.kyoto-u.ac.jp/kp/index.html) and Dst and AE indices (https://wdc.kugi.kyoto-u.ac.jp/dstae/index.html). Pedersen conductivity used in this study was computed from the ionospheric conductivity model, height profile (https://wdc.kugi.kyoto-u.ac.jp/ionocond/exp/icexp.html).

Acknowledgments

The financial assistance of the National Research Foundation (NRF) (the grant number: 144832) towards this research is hereby acknowledged. Opinions expressed and conclusions arrived at, are those of the authors and are not necessarily to be attributed to the NRF. This work is jointly supported by the Sino-South Africa Joint Research on Polar Space Environment (the grant number: 2021YFE0106400).

The Zhongshan SuperDARN radar is maintained and operated by the Polar Research Institute of China. We acknowledge the use of SuperDARN data. SuperDARN is a network of radars funded by national scientific funding agencies of Australia, Canada, China, France, Italy, Japan, Norway, South Africa, the United Kingdom, and the United States of America. We thank the PI of the Zhongshan SuperDARN radar Dr Hongqiao Hu for consenting to our use of the Zhongshan data which is funded by Polar Research Institute of China. We would like to acknowledge the Chinese Meridian Project and Chinese National Polar Scientific Data Center for allowing us to use the Zhongshan radar data.

We thank the reviewers team that helped us to evaluate and improve this study.

References

Atilaw, T. Y., Stephenson, J. A., & Katamzi-Joseph, Z. T. (2021). Multitaper analysis of an MSTID event above Antarctica on 17 March 2013. *Polar Science*,

100643. doi: https://doi.org/10.1016/j.polar.2021.100643
Bristow, W., & Greenwald, R. (1997). On the spectrum of thermospheric gravity waves observed by the Super Dual Auroral Radar Network. *Journal of Geophysical Research: Space Physics*, *102*(A6), 11585–11595. doi: https://doi.org/10.1029/97JA00515
Buneman, O. (1963). Excitation of field aligned sound waves by electron streams. *Physical Review Letters*, *10*(7), 285. doi: https://doi.org/10.1103/PhysRevLett.10.285
Chisham, G., Lester, M., Milan, S. E., Freeman, M., Bristow, W., Grocott, A., ... others (2007). A decade of the Super Dual Auroral Radar Network (SuperDARN): Scientific achievements, new techniques and future directions. *Surveys in Geophysics*, *28*(1), 33–109. doi: https://doi.org/10.1007/s10712-007-9017-8
Chisham, G., Yeoman, T. K., & Sofko, G. (2008). Mapping ionospheric backscatter measured by the SuperDARN HF radars–part 1: A new empirical virtual height model. In *Annales geophysicae* (Vol. 26, pp. 823–841). doi: https://doi.org/10.5194/angeo-26-823-2008
Chou, M.-Y., Lin, C. C., Yue, J., Chang, L. C., Tsai, H.-F., & Chen, C.-H. (2017). Medium-scale traveling ionospheric disturbances triggered by Super Typhoon Nepartak (2016). *Geophysical Research Letters*, *44*(15), 7569–7577. doi: https://doi.org/10.1002/2017GL073961
Cosgrove, R. (2007). Generation of mesoscale F layer structure and electric fields by the combined Perkins and E s layer instabilities, in simulations. In *Annales geophysicae* (Vol. 25, pp. 1579–1601). doi: https://doi.org/10.5194/angeo-25-1579-2007
Crowley, G., & Rodrigues, F. (2012). Characteristics of traveling ionospheric disturbances observed by the TIDDBIT sounder. *Radio Science*, *47*(04), 1–12. doi: https://doi.org/10.1029/2011RS004959
Currie, J., Waters, C., Menk, F., Sciffer, M., & Bristow, W. (2016). SuperDARN backscatter during intense geomagnetic storms. *Radio Science*, *51*(6), 814–825. doi: https://doi.org/10.1002/2016RS005960
Danskin, D., Koustov, A., Ogawa, T., Nishitani, N., Nozawa, S., Milan, S., ... Andre, D. (2002). On the factors controlling occurrence of F-region coherent echoes. In *Annales geophysicae* (Vol. 20, pp. 1385–1397). doi: https://doi.org/10.5194/angeo-20-1385-2002
Dimant, Y. S., & Oppenheim, M. (2004). Ion thermal effects on E-region instabilities: linear theory. *Journal of atmospheric and solar-terrestrial physics*, *66*(17), 1639–1654. doi: https://doi.org/10.1016/j.jastp.2004.07.006
Dimant, Y. S., & Sudan, R. (1995). Kinetic theory of the Farley-Buneman instability in the E region of the ionosphere. *Journal of Geophysical Research: Space Physics*, *100*(A8), 14605–14623. doi: https://doi.org/10.1029/95JA00794
Drexler, J., & St-Maurice, J.-P. (2005). A possible origin for large aspect angle (HAIR) echoes seen by SuperDARN radars in the E region. In *Annales geophysicae* (Vol. 23, pp. 767–772). doi: https://doi.org/10.5194/angeo-23-767-2005
Farley Jr, D. (1963). A plasma instability resulting in field-aligned irregularities in the ionosphere. *Journal of Geophysical Research*, *68*(22), 6083–6097. doi: https://doi.org/10.1029/JZ068i022p06083
Fejer, B. G., & Kelley, M. (1980). Ionospheric irregularities. *Reviews of Geophysics*, *18*(2), 401–454. doi: https://doi.org/10.1029/RG018i002p00401
Forsythe, V. V., & Makarevich, R. A. (2017). Global view of the E region irregularity and convection velocities in the high-latitude Southern Hemisphere. *Journal of Geophysical Research: Space Physics*, *122*(2), 2467–2483. doi: https://doi.org/10.1002/2016JA023711
Francis, S. H. (1974). A theory of medium-scale traveling ionospheric disturbances. *Journal of Geophysical Research*, *79*(34), 5245–5260. doi: https://doi.org/10

.1029/JA079i034p05245

Frissell, N., Baker, J., Ruohoniemi, J., Gerrard, A., Miller, E., Marini, J., ... Bristow, W. (2014). Climatology of medium-scale traveling ionospheric disturbances observed by the midlatitude Blackstone SuperDARN radar. *Journal of Geophysical Research: Space Physics*, *119*(9), 7679–7697. doi: https://doi.org/10.1002/2014JA019870

Galushko, V., Paznukhov, V., Sopin, A., & Yampolski, Y. (2016). Statistics of ionospheric disturbances over the Antarctic Peninsula as derived from TEC measurements. *Journal of Geophysical Research: Space Physics*, *121*(4), 3395–3409. doi: https://doi.org/10.1002/2015JA022302

Galushko, V., Paznukhov, V., Yampolski, Y., & Foster, J. (1998). Incoherent scatter radar observations of AGW/TID events generated by the moving solar terminator. *Annales Geophysicae*, *16*(7), 821–827. doi: https://doi.org/10.1007/s005850050651

Greenwald, R., Baker, K., Dudeney, J., Pinnock, M., Jones, T., Thomas, E., ... others (1995). Darn/superdarn. *Space Science Reviews*, *71*(1-4), 761–796. doi: https://doi.org/10.1007/BF00751350

Grocott, A., Hosokawa, K., Ishida, T., Lester, M., Milan, S. E., Freeman, M., et al. (2013). Characteristics of medium-scale traveling ionospheric disturbances observed near the Antarctic Peninsula by HF radar. *Journal of Geophysical Research: Space Physics*, *118*(9), 5830–5841. doi: https://doi.org/10.1002/jgra.50515

Haldoupis, C., Kelley, M. C., Hussey, G. C., & Shalimov, S. (2003). Role of unstable sporadic-E layers in the generation of midlatitude spread F. *Journal of Geophysical Research: Space Physics*, *108*(A12). doi: https://doi.org/10.1029/2003JA009956

Haldoupis, C., Schlegel, K., & Hussey, G. (2000). Auroral E-region electron density gradients measured with EISCAT. *Annales Geophysicae*, *18*(9), 1172–1181. doi: https://doi.org/10.1007/s005850000223

Hall, G., MacDougall, J., Cecile, J.-F., Moorcroft, D., & St.-Maurice, J. (1999). Finding gravity wave source positions using the Super Dual Auroral Radar Network. *Journal of Geophysical Research: Space Physics*, *104*(A1), 67–78. doi: https://doi.org/10.1029/98JA02830

Hall, G., MacDougall, J., Moorcroft, D., St.-Maurice, J.-P., Manson, A., & Meek, C. (1997). Super dual auroral radar network observations of meteor echoes. *Journal of Geophysical Research: Space Physics*, *102*(A7), 14603–14614. doi: https://doi.org/10.1029/97JA00517

Hamza, A. (1999). Perkins instability revisited. *Journal of Geophysical Research: Space Physics*, *104*(A10), 22567–22575. doi: https://doi.org/10.1029/1999JA900307

Hamza, A., & St-Maurice, J.-P. (1993). A turbulent theoretical framework for the study of current-driven E region irregularities at high latitudes: Basic derivation and application to gradient-free situations. *Journal of Geophysical Research: Space Physics*, *98*(A7), 11587–11599. doi: https://doi.org/10.1029/92JA02836

Hazeyama, W., Nishitani, N., Hori, T., Nakamura, T., & Perwitasari, S. (2022). Statistical study of seasonal and solar activity dependence of nighttime mstids occurrence using the superdarn hokkaido pair of radars. *Journal of Geophysical Research: Space Physics*, *127*(4), e2021JA029965. doi: https://doi.org/10.1029/2021JA029965

He, L.-S., Dyson, P., Parkinson, M., & Wan, W. (2004). Studies of medium scale travelling ionospheric disturbances using TIGER SuperDARN radar sea echo observations. In *Annales geophysicae* (Vol. 22, pp. 4077–4088). doi: https://doi.org/10.5194/angeo-22-4077-2004

Hernández-Pajares, M., Juan, J. M., & Sanz, J. (2006). Medium-scale traveling ionospheric disturbances affecting GPS measurements: Spatial and temporal analysis. *Journal of Geophysical Research: Space Physics*, *111*(A7). doi: https://doi.org/10.1029/2005JA011474

Hiyadutuje, A., Habarulema, J. B., Kosch, M. J., Chen, X., Stephenson, J., & Matamba, T. M. (2023). *Data on the simultaneous occurrence of traveling ionospheric disturbances, farley buneman and gradient drift instabilities observed by the zhongshan superdarn hf radar* (Vol. V2). Mendeley Data. (data retrieved on 02/06/2022 - 25/07/2023 from the Virginia Tech website, `http://vt.superdarn.org/`) doi: https://doi.org/10.17632/9skd2fw4yy.1

Hiyadutuje, A., Kosch, M. J., & Stephenson, J. A. (2022). First observations of E-region Near Range Echoes partially modulated by F-region Traveling Ionospheric Disturbances observed by the same SuperDARN HF radar. *Journal of Geophysical Research: Space Physics*, *127*, e2021JA030157. doi: https://doi.org/10.1029/2021JA030157

Hocke, K., Schlegel, K., et al. (1996). A review of atmospheric gravity waves and travelling ionospheric disturbances: 1982–1995. *Annales Geophysicae*, *14*(9), 917. doi: https://doi.org/10.1007/s00585-996-0917-6

Hunsucker, R. D. (1982). Atmospheric gravity waves generated in the high-latitude ionosphere: A review. *Reviews of Geophysics*, *20*(2), 293–315. doi: https://doi.org/10.1029/RG020i002p00293

Hussey, G., Meek, C., André, D., Manson, A., Sofko, G., & Hall, C. (2000). A comparison of Northern Hemisphere winds using SuperDARN meteor trail and MF radar wind measurements. *Journal of Geophysical Research: Atmospheres*, *105*(D14), 18053–18066. doi: https://doi.org/10.1029/2000JD900272

Ishida, T., Hosokawa, K., Shibata, T., Suzuki, S., Nishitani, N., & Ogawa, T. (2008). SuperDARN observations of daytime MSTIDs in the auroral and mid-latitudes: Possibility of long-distance propagation. *Geophysical Research Letters*, *35*(13). doi: https://doi.org/10.1029/2008GL034623

Ivarsen, M. F., St-Maurice, J.-P., Hussey, G., Spicher, A., Jin, Y., Lozinsky, A., et al. (2023). Measuring small-scale plasma irregularities in the high-latitude E-and F-regions simultaneously. *Scientific Reports*, *13*(1), 11579. doi: https://doi.org/10.1038/s41598-023-38777-4

Iyemori, T., & Rao, D. (1996). Decay of the Dst field of geomagnetic disturbance after substorm onset and its implication to storm-substorm relation. *Annales Geophysicae*, *14*(4), 608–618. doi: https://doi.org/10.1007/s00585-996-0608-3

Jenkins, B., & Jarvis, M. J. (1999). Mesospheric winds derived from SuperDARN HF radar meteor echoes at Halley, Antarctica. *Earth, planets and space*, *51*(7-8), 685–689. doi: https://doi.org/10.1186/BF03353226

John, P., & Saxena, Y. (1975). Observation of the Farley-Buneman instability in laboratory plasma. *Geophysical Research Letters*, *2*(6), 251–254. doi: https://doi.org/10.1029/GL002i006p00251

Kaminskyi, R., Kunanets, N., Pasichnyk, V., Rzheuskyi, A., & Khudyi, A. (2018). Recovery Gaps in Experimental Data. In *Colins* (pp. 108–118). doi: http://ceur-ws.org/Vol-2136/10000108.pdf

Kelley, Kunduri, B., Baker, J., Ruohoniemi, J., & Shepherd, S. (2023). Storm Time Electrified MSTIDs Observed Over Mid-Latitude North America. *Journal of Geophysical Research: Space Physics*, *128*(3), e2022JA031115. doi: https://doi.org/10.1029/2022JA031115

Kelley, M. C. (2009). *The Earth's ionosphere: plasma physics and electrodynamics.* Academic press.

Kelly, M. (2012). *The Earth's ionosphere: Plasma physics and electrodynamics* (Vol. 43). Elsevier.

Kirkwood, S., & Nilsson, H. (2000). High-latitude sporadic-E and other thin layers– the role of magnetospheric electric fields. *Space science reviews*, *91*(3), 579–613. doi: https://doi.org/10.1023/A:1005241931650

Kissack, R., Kagan, L., & St-Maurice, J.-P. (2008). Thermal effects on Farley–Buneman waves at nonzero aspect and flow angles. I. dispersion relation. *Physics of Plasmas*, *15*(2). doi: https://doi.org/10.1063/1.2834275

Kissack, R., St.-Maurice, J.-P., & Moorcroft, D. (1997). The effect of electron-neutral energy exchange on the fluid Farley-Buneman instability threshold. *Journal of Geophysical Research: Space Physics*, *102*(A11), 24091–24115. doi: https://doi.org/10.1029/95JA00794

Kotake, N., Otsuka, Y., Ogawa, T., Tsugawa, T., & Saito, A. (2007). Statistical study of medium-scale traveling ionospheric disturbances observed with the GPS networks in Southern California. *Earth, planets and space*, *59*(2), 95–102. doi: https://doi.org/10.1186/BF03352681

Kotake, N., Otsuka, Y., Tsugawa, T., Ogawa, T., & Saito, A. (2006). Climatological study of GPS total electron content variations caused by medium-scale traveling ionospheric disturbances. *Journal of Geophysical Research: Space Physics*, *111*(A4). doi: https://doi.org/10.1029/2005JA011418

Kovalev, D., Smirnov, A., & Dimant, Y. (2008). Modeling of the Farley-Buneman instability in the E-region ionosphere: a new hybrid approach. In *Annales geophysicae* (Vol. 26, pp. 2853–2870). doi: https://doi.org/10.5194/angeo-26-2853-2008

Liu, Y., Zhou, C., Tang, Q., Kong, J., Gu, X., Ni, B., … Zhao, Z. (2019). Evidence of Mid-and Low-Latitude Nighttime Ionospheric *E*–*F* Coupling: Coordinated Observations of Sporadic *E* layers, *F*-region Field-Aligned Irregularities, and Medium-Scale Traveling Ionospheric Disturbances. *IEEE Transactions on Geoscience and Remote Sensing*, *57*(10), 7547–7557. doi: https://doi.org/10.1109/TGRS.2019.2914059

Loewe, C., & Prölss, G. (1997). Classification and mean behavior of magnetic storms. *Journal of Geophysical Research: Space Physics*, *102*(A7), 14209–14213. doi: https://doi.org/10.1029/96JA04020

Makarevich, R. A. (2016). Toward an integrated view of ionospheric plasma instabilities: Altitudinal transitions and strong gradient case. *Journal of Geophysical Research: Space Physics*, *121*(4), 3634–3647. doi: https://doi.org/10.1002/2016JA022515

Makarevich, R. A. (2021). Toward an integrated view of ionospheric plasma instabilities: 6. analytic analysis of thermal effects. *Journal of Geophysical Research: Space Physics*, *126*(9), e2021JA029178. doi: https://doi.org/10.1029/2021JA029178

Martinis, C., Baumgardner, J., Wroten, J., & Mendillo, M. (2010). Seasonal dependence of MSTIDs obtained from 630.0 nm airglow imaging at Arecibo. *Geophysical Research Letters*, *37*(11). doi: https://doi.org/10.1029/2010GL043569

Milan, S. E., & Lester, M. (2001). A classification of spectral populations observed in HF radar backscatter from the E region auroral electrojets. In *Annales geophysicae* (Vol. 19, pp. 189–204). doi: https://doi.org/10.5194/angeo-19-189-2001

Milan, S. E., Lester, M., Yeoman, T., Robinson, T., Uspensky, M., & Villain, J.-P. (2004). HF radar observations of high-aspect angle backscatter from the E-region. In *Annales geophysicae* (Vol. 22, pp. 829–847). doi: https://doi.org/10.5194/angeo-22-829-2004

Miyoshi, Y., Jin, H., Fujiwara, H., & Shinagawa, H. (2018). Numerical study of traveling ionospheric disturbances generated by an upward propagating gravity wave. *Journal of Geophysical Research: Space Physics*, *123*(3), 2141–2155. doi: https://doi.org/10.1002/2017JA025110

Nygrén, T., Aikio, A., Voiculescu, M., & Cai, L. (2015). Radar observations of simultaneous traveling ionospheric disturbances and atmospheric gravity waves. *Journal of Geophysical Research: Space Physics*, *120*(5), 3949–3960. doi:

https://doi.org/10.1002/2014JA020794

Ogawa, T., Igarashi, K., Aikyo, K., & Maeno, H. (1987). NNSS satellite observations of medium-scale traveling ionospheric disturbances at southern high-latitudes. *Journal of geomagnetism and geoelectricity*, *39*(12), 709–721. doi: https://doi.org/10.5636/jgg.39.709

Ogawa, T., Nishitani, N., Otsuka, Y., Shiokawa, K., Tsugawa, T., & Hosokawa, K. (2009). Medium-scale traveling ionospheric disturbances observed with the SuperDARN Hokkaido radar, all-sky imager, and GPS network and their relation to concurrent sporadic E irregularities. *Journal of Geophysical Research: Space Physics*, *114*(A3), A03316. doi: https://doi.org/10.1029/2008JA013893

Ogawa, T., Nishitani, N., Sato, N., Yamagishi, H., & Yukimatu, A. S. (2002). Upper mesosphere summer echoes detected with the Antarctic Syowa HF radar. *Geophysical research letters*, *29*(7), 61–1. doi: https://doi.org/10.1029/2001GL014094

Oppenheim, M., & Dimant, Y. S. (2013). Kinetic simulations of 3-D Farley-Buneman turbulence and anomalous electron heating. *Journal of Geophysical Research: Space Physics*, *118*(3), 1306–1318. doi: https://doi.org/10.1002/jgra.50196

Otani, N. F., & Oppenheim, M. (2006). Saturation of the Farley-Buneman instability via three-mode coupling. *Journal of Geophysical Research: Space Physics*, *111*(A3). doi: https://doi.org/10.1029/2005JA011215

Otsuka, Y., Onoma, F., Shiokawa, K., Ogawa, T., Yamamoto, M., & Fukao, S. (2007). Simultaneous observations of nighttime medium-scale traveling ionospheric disturbances and E region field-aligned irregularities at midlatitude. *Journal of Geophysical Research: Space Physics*, *112*(A6). doi: https://doi.org/10.1029/2005JA011548

Otsuka, Y., Shinbori, A., Tsugawa, T., & Nishioka, M. (2021). Solar activity dependence of medium-scale traveling ionospheric disturbances using GPS receivers in Japan. *Earth, Planets and Space*, *73*(1), 1–11. doi: https://doi.org/10.1186/s40623-020-01353-5

Otsuka, Y., Shiokawa, K., Ogawa, T., Yokoyama, T., & Yamamoto, M. (2009). Spatial relationship of nighttime medium-scale traveling ionospheric disturbances and f region field-aligned irregularities observed with two spaced all-sky airglow imagers and the middle and upper atmosphere radar. *Journal of Geophysical Research: Space Physics*, *114*(A5). doi: https://doi.org/10.1029/2008JA013902

Otsuka, Y., Suzuki, K., Nakagawa, S., Nishioka, M., Shiokawa, K., & Tsugawa, a. (2013). GPS observations of medium-scale traveling ionospheric disturbances over Europe. In *Annales geophysicae* (Vol. 31, pp. 163–172). doi: https://doi.org/10.5194/angeo-31-163-2013

Perkins, F. (1973). Spread F and ionospheric currents. *Journal of Geophysical Research*, *78*(1), 218–226. doi: https://doi.org/10.1029/JA078i001p00218

Ponomarenko, P., Iserhienrhien, B., & Maurice, J.-P. S. (2016). Morphology and possible origins of near-range oblique HF backscatter at high and midlatitudes. *Radio Science*, *51*(6), 718–730. doi: https://doi.org/10.1002/2016RS006088

Ponomarenko, P., Nishitani, N., Oinats, A. V., Tsuya, T., & St-Maurice, J.-P. (2015). Application of ground scatter returns for calibration of hf interferometry data. *Earth, Planets and Space*, *67*(1), 1–9. doi: https://doi.org/10.1186/s40623-015-0310-3

Ponomarenko, P., St-Maurice, J., Waters, C., Gillies, R., & Koustov, A. (2009). Refractive index effects on the scatter volume location and Doppler velocity estimates of ionospheric HF backscatter echoes. In *Annales geophysicae: atmospheres, hydrospheres and space sciences* (Vol. 27, p. 4207). doi: https://doi.org/10.5194/angeo-27-4207-2009

Rauf, A., Li, H., Ullah, S., Meng, L., Wang, B., & Wang, M. (2019). Investigation of PMSE dependence on high energy particle precipitation during their simultaneous occurrence. *Advances in Space Research*, *63*(1), 309–316. doi: https://doi.org/10.1016/j.asr.2018.09.007

Robinson, R., Zanetti, L., Anderson, B., Vines, S., & Gjerloev, J. (2021). Determination of auroral electrodynamic parameters from ampere field-aligned current measurements. *Space weather*, *19*(4), e2020SW002677. doi: https://doi.org/10.1029/2020SW002677

Rojas, E., & Hysell, D. (2021). Hybrid Plasma Simulations of Farley-Buneman Instabilities in the Auroral E-Region. *Journal of Geophysical Research: Space Physics*, *126*(5), e2020JA028379. doi: https://doi.org/10.1029/2020JA028379

Ruohoniemi, J., & Baker, K. (1998). Large-scale imaging of high-latitude convection with Super Dual Auroral Radar Network HF radar observations. *Journal of Geophysical Research: Space Physics*, *103*(A9), 20797–20811. doi: https://doi.org/10.1029/98JA01288

Sahr, J. D., & Fejer, B. G. (1996). Auroral electrojet plasma irregularity theory and experiment: A critical review of present understanding and future directions. *Journal of Geophysical Research: Space Physics*, *101*(A12), 26893–26909. doi: https://doi.org/10.1029/96JA02404

Samson, J., Greenwald, R., Ruohoniemi, J., Frey, A., & Baker, K. (1990). Goose Bay radar observations of Earth-reflected, atmospheric gravity waves in the high-latitude ionosphere. *Journal of Geophysical Research: Space Physics*, *95*(A6), 7693–7709. doi: https://doi.org/10.1029/JA095iA06p07693

Sato, T. (1973). Unified theory of type I and II irregularities in the equatorial electrojet. *Journal of Geophysical Research*, *78*(13), 2232–2243. doi: https://doi.org/10.1029/JA078i013p02232

Shepherd, S., & Ruohoniemi, J. (2000). Electrostatic potential patterns in the high-latitude ionosphere constrained by SuperDARN measurements. *Journal of Geophysical Research: Space Physics*, *105*(A10), 23005–23014. doi: https://doi.org/10.1029/2000JA000171

St.-Maurice, J.-P. (1985). A nonlocal theory of the high-latitude Farley-Buneman instability. *Journal of Geophysical Research: Space Physics*, *90*(A6), 5211–5225. doi: https://doi.org/10.1029/JA090iA06p05211

St.-Maurice, J.-P., & Chau, J. L. (2016). A theoretical framework for the changing spectral properties of meter-scale Farley-Buneman waves between 90 and 125 km altitudes. *Journal of Geophysical Research: Space Physics*, *121*(10), 10–341. doi: https://doi.org/10.1002/2016JA023105

St.-Maurice, J.-P., & Hamza, A. (2001). A new nonlinear approach to the theory of E region irregularities. *Journal of Geophysical Research: Space Physics*, *106*(A2), 1751–1759. doi: https://doi.org/10.1029/2000JA000246

St.-Maurice, J.-P., Hanuise, C., & Kudeki, E. (1986). On the dependence of the phase velocity of equatorial irregularities on the polarization electric field and theoretical implications. *Journal of Geophysical Research: Space Physics*, *91*(A12), 13493–13505. doi: https://doi.org/10.1029/JA091iA12p13493

St-Maurice, J.-P., Huyghebaert, D., Ivarsen, M. F., & Hussey, G. C. (2023). Narrow Width Farley-Buneman Spectra Above 100 km Altitude. *Journal of Geophysical Research: Space Physics*, *128*(10), e2022JA031191. doi: https://doi.org/10.1029/2022JA031191

St.-Maurice, J.-P., & Nishitani, N. (2020). On the Origin of Far-Aspect Angle Irregularity Regions Seen by HF Radars at 100-km Altitude. *Journal of Geophysical Research: Space Physics*, *125*(6), e2019JA027473. doi: https://doi.org/10.1029/2019JA027473

St.-Maurice, J.-P., Prikryl, P., Danskin, D., Hamza, A., Sofko, G., Koehler, J., ... Chen, J. (1994). On the origin of narrow non-ion-acoustic coherent radar spectra in the high-latitude E region. *Journal of Geophysical Research: Space Physics*, *99*(A4), 6447–6474. doi: https://doi.org/10.1029/93JA02353

Sun, L., Xu, J., Wang, W., Yue, X., Yuan, W., Ning, B., et al. (2015). Mesoscale field-aligned irregularity structures (FAIs) of airglow associated with medium-scale traveling ionospheric disturbances (MSTIDs). *Journal of Geophysical Research: Space Physics*, *120*(11), 9839–9858. doi: https://doi.org/10.1002/2014JA020944

Suzuki, S., Hosokawa, K., Otsuka, Y., Shiokawa, K., Ogawa, T., Nishitani, N., et al. (2009). Coordinated observations of nighttime medium-scale traveling ionospheric disturbances in 630-nm airglow and HF radar echoes at mid-latitudes. *Journal of Geophysical Research: Space Physics*, *114*(A7). doi: https://doi.org/10.1029/2008JA013963

Tsuchiya, S., Shiokawa, K., Fujinami, H., Otsuka, Y., Nakamura, T., Connors, M., et al. (2019). Three-dimensional Fourier analysis of the phase velocity distributions of mesospheric and ionospheric waves based on airglow images collected over 10 years: Comparison of Magadan, Russia, and Athabasca, Canada. *Journal of Geophysical Research: Space Physics*, *124*(10), 8110–8124. doi: https://doi.org/10.1029/2019JA026783

Tsugawa, T., Kotake, N., Otsuka, Y., & Saito, A. (2007). Medium-scale traveling ionospheric disturbances observed by GPS receiver network in Japan: A short review. *GPS Solutions*, *11*(2), 139–144. doi: https://doi.org/10.1007/s10291-006-0045-5

Tsugawa, T., Saito, A., & Otsuka, Y. (2004). A statistical study of large-scale traveling ionospheric disturbances using the GPS network in Japan. *Journal of Geophysical Research: Space Physics*, *109*(A6). doi: https://doi.org/10.1029/2003JA010302

Valladares, C. E., & Hei, M. A. (2012). Measurement of the characteristics of TIDs using small and regional networks of GPS receivers during the campaign of 17–30 July of 2008. *International Journal of Geophysics*, *2012*. doi: https://doi.org/10.1155/2012/548784

Van Camp, M., & Vauterin, P. (2005). Tsoft: graphical and interactive software for the analysis of time series and Earth tides. *Computers & Geosciences*, *31*(5), 631–640. doi: https://doi.org/10.1016/j.cageo.2004.11.015

Vickrey, J. F., & Kelley, M. C. (1982). The effects of a conducting E layer on classical F region cross-field plasma diffusion. *Journal of Geophysical Research: Space Physics*, *87*(A6), 4461–4468. doi: https://doi.org/10.1029/JA087iA06p04461

Vlasov, A., Kauristie, K., Van de Kamp, M., Luntama, J.-P., & Pogoreltsev, A. (2011). A study of traveling ionospheric disturbances and atmospheric gravity waves using EISCAT Svalbard Radar IPY-data. In *Annales geophysicae* (Vol. 29, pp. 2101–2116). doi: https://doi.org/10.5194/angeo-29-2101-2011

Ware, J. H., Mosteller, F., Delgado, F., Donnelly, C., & Ingelfinger, J. A. (2019). P values. In *Medical uses of statistics* (pp. 181–200). CRC Press. doi: https://doi.org/10.1201/9780429187445-10

Wilks, D. S. (2011). *Statistical methods in the atmospheric sciences* (Vol. 100). Academic press.

Young, M. A., Oppenheim, M. M., & Dimant, Y. S. (2017). Hybrid simulations of coupled Farley-Buneman/gradient drift instabilities in the equatorial E region ionosphere. *Journal of Geophysical Research: Space Physics*, *122*(5), 5768–5781. doi: https://doi.org/10.1002/2017JA024161

Young, M. A., Oppenheim, M. M., & Dimant, Y. S. (2019). Simulations of secondary Farley-Buneman instability driven by a kilometer-scale primary wave: Anomalous transport and formation of flat-topped electric fields. *Journal of Geophysical Research: Space Physics*, *124*(1), 734–748. doi: https://doi.org/10.1029/2018JA026072

Zou, K. H., Tuncali, K., & Silverman, S. G. (2003). Correlation and simple linear regression. *Radiology*, *227*(3), 617–628. doi: https://doi.org/10.1148/radiol

.2273011499